JOURNAL OF PETROLOGY | VOLUME 48 | NUMBER 2 | PAGES 271–302 | 2007 | doi:10.1093/petrology/egl060

Polymetamorphic Evolution of the Trans-Hudson Orogen, Baffin Island, Canada: Integration of Petrological, Structural and Geochronological Data

M. R. ST-ONGE*, N. WODICKA AND O. IJEWLIW

GEOLOGICAL SURVEY OF CANADA, 601 BOOTH STREET, OTTAWA, ONTARIO, CANADA, K1A 0E8

**RECEIVED MAY 26, 2005; ACCEPTED SEPTEMBER 21, 2006;
ADVANCE ACCESS PUBLICATION NOVEMBER 3, 2006**

Supracrustal units metamorphosed at mid-crustal conditions within the Paleoproterozoic Trans-Hudson Orogen are preserved within an obliquely exposed continental collision zone on Baffin Island (Canada). Early granulite-facies assemblages yield thermobarometric data and phase diagram information that define a steep, compressive P–T *path segment. These assemblages are bracketed between ca. 1849 and 1835 Ma, and are interpreted to result from (1) heat advection by an 1865 +4/–2 to 1848 ± 2 Ma Andean-type granitic batholith, and (2) a* ca. *1845 Ma crustal thickening event associated with accretion of an intra-oceanic arc terrane. A subsequent regional metamorphic event is characterized by the growth of retrograde, upper amphibolite-facies assemblages that define a clockwise, decompressive* P–T *path. Mineral growth is bracketed between 1820 ± 1 and 1813 ± 2 Ma, and is localized within deformation zones associated with the 1820 +4/–3 to 1795 ± 2 Ma collision of the Rae and Superior cratons. The metamorphic history of Baffin Island supports a progressive change from plate-margin to intraplate processes within an evolving convergent orogen during the Paleoproterozoic that is similar to those documented in younger collisional belts.*

KEY WORDS: *polymetamorphism; geochronology; Paleoproterozoic; Trans-Hudson Orogen*

INTRODUCTION

Building on the innovative work of England & Thompson (1984), regional metamorphism in convergent orogens has been shown by coupled thermal–mechanical models to result from the complex interplay of several, generally causative, probably interlinked processes that include subduction-driven convergence and tectonic accretion or collision, crustal thickening and deformation, structural and/or erosional exhumation, underthrusting of materials rich in radiogenic heat-producing elements, and magmatic heat advection (e.g. Jamieson *et al.*, 1996, 1998, 2002; Huerta *et al.*, 1998, 1999; and references therein). Concurrently, field-based petrological–structural–thermochronological studies have successfully documented the fundamental polymetamorphic character of many higher-grade terrains within collisional orogenic belts ranging in age from Eocene to Neoproterozoic (e.g. Jamieson *et al.*, 1995; Vannay & Hodges, 1996; Culshaw *et al.*, 1997; Harrison *et al.*, 1997; Moecher, 1999; Searle *et al.*, 1999, 2003; Walker *et al.*, 1999; Carr *et al.*, 2000; Indares *et al.*, 2000; Wodicka *et al.*, 2000; Fraser *et al.*, 2001; Johnson *et al.*, 2003).

In this paper, we extend the field-based integrated petrological–structural–thermochronological study of convergent orogens to the Paleoproterozoic, and are able to relate key petrological aspects of polymetamorphic mineral assemblages to a well-constrained history of crustal deformation and evolution. The focus of our work is a part of southern Baffin Island (Nunavut, Canada) where an oblique crustal cross-section through a continental collision zone of Paleoproterozoic age is superbly preserved and exposed (St-Onge *et al.*, 2002). The exceptional tectonic context afforded by the geology of southern Baffin Island allows for the internally consistent correlation of deformation fabrics, polymetamorphic assemblages,

*Corresponding author. Telephone: (613) 995-4935. Fax: (613) 943-5318. E-mail: mstonge@nrcan.gc.ca

© The Author 2006. Published by Oxford University Press. All rights reserved. For Permissions, please email: journals.permissions@oxfordjournals.org

Downloaded from http://petrology.oxfordjournals.org/ by guest on June 7, 2013

mineral chemistry, and age data. The correlation of these multiple datasets for southern Baffin Island, as presented in this paper, allows us to propose unambiguous links between thermal events or processes and consequent regional metamorphic associations.

We begin by providing the regional tectonic context for our work and describing the main crustal components of the Quebec–Baffin segment of the Himalayan-scale Trans-Hudson Orogen. The large amount of published work pertaining to this Paleoproterozoic collisional orogen (St-Onge *et al.*, 1992, 1999*a*, 2001, 2002; Scott *et al.*, 2003; and references therein) provides us with the context within which we can evaluate the significance of the detailed petrological and thermochronological data presented here and which is specific to the generally less well understood orogenic internal zone. Key structural and petrological observations outline the deformation and metamorphic histories of the southern Baffin Island area. Integrated thermobarometric, phase diagram, and thermochronological work documents the pressure–temperature–time–deformation history of the polymetamorphic internal zone of the Trans-Hudson Orogen on Baffin Island. These results distinguish two regionally significant metamorphic events (M_{1a}, M_2) and document the thermal evolution of crustal rocks in the hanging wall of a major suture (tectonic zone separating two crustal blocks of contrasting geological history and parentage or provenance) during accretion- and collision-related deformation. We conclude by considering the potential implications of the south Baffin Island results for the thermal evolution of convergent to collisional orogenic belts.

GEOLOGICAL BACKGROUND

The Trans-Hudson Orogen (Hoffman, 1988; Lewry & Collerson, 1990) is a Himalayan-scale collisional orogenic belt that extends from the south–central part of the North American continent to its northeastern edge, where it is truncated by the younger Meso- to Neoproterozoic Grenville Orogen (Fig. 1). The Trans-Hudson Orogen separates a partially subducted or underthrust collisional lower plate (the Superior craton) from a collisional upper-plate (assembled in the hanging wall of a subduction zone) collage of Archean crustal blocks that includes the Wyoming craton, the Hearne domain and Rae craton of the northern Churchill plate, and the North Atlantic craton of Labrador and Greenland (Fig. 1). The orogen is over 4600 km in strike-length and, in certain segments, over 800 km in strike-width. Beyond North America it has been correlated (Zhao *et al.*, 2002) with the Nagssugtoqidian Orogen of Greenland, the Kola–Karelia Orogen of the Baltic Shield, and possibly with the Transantarctic Orogen of Eastern Antarctica.

Recently, Searle & St-Onge (2004) and St-Onge & Searle (2004) have argued that the tectonic record of the Trans-Hudson Orogen in the late Paleoproterozoic (*ca.* 1820–1795 Ma) was similar to the record of collision and indentation of India into SE Asia in the Eocene (beginning at *ca.* 50.6 Ma; Rowley *et al.*, 2004). An overview of the tectonostratigraphic framework of the Quebec–Baffin segment of Trans-Hudson Orogen is given below from south to north (St-Onge *et al.*, 2002; Scott *et al.*, 2003, and references therein), to provide a regional context for the southern Baffin Island study area (Fig. 2).

Lower-plate cratonic margin

In northern Quebec, the exposed lower-plate Archean Superior craton (Fig. 2) comprises dominantly felsic orthogneisses and plutonic units ranging in age between $3220 + 32/-23$ and 2737 ± 2 Ma (Fig. 3; Parrish, 1989, unpublished data; St-Onge *et al.*, 1992; Scott & St-Onge, 1995). Unconformably overlying the felsic basement is a suite of parautochthonous sedimentary strata, continental tholeiitic flood basalt and rhyolite (Povungnituk Group, Figs 2 and 4a) associated with initial Paleoproterozoic rifting of the northern Superior craton and yielding ages between $2038 + 4/-2$ and $1959 + 3{\cdot}1/-2{\cdot}7$ Ma (Fig. 3; Parrish, 1989; Machado *et al.*, 1993). Overlying the initial rift sedimentary and volcanic rocks is a younger succession of predominantly Mg-rich komatiitic to tholeiitic basalts (Chukotat Group, Figs 2 and 4a) accumulated during renewed rifting along the northern continental margin (St-Onge *et al.*, 2000a) and dated between $1887 + 37/-11$ and 1870 ± 4 Ma (Fig. 3; Wodicka *et al.*, 2002a; R. R. Parrish, unpublished data).

Ophiolitic and magmatic arc assemblages

A major tectonic boundary or crustal suture (Bergeron suture, Figs 2 and 4e; St-Onge *et al.*, 2001), which accommodated displacements to the south, separates the Superior margin strata (described above) from allochthonous northern crustal elements. Accreted units in the hanging wall of the Bergeron suture include (Figs 2 and 4): (1) an ophiolite (Watts Group) dated to 1998 ± 2 Ma (Fig. 3; Parrish, 1989); (2) a fore-arc clastic sequence (Spartan Group), which is undated; and (3) a magmatic arc terrane (Parent Group and Narsajuaq arc). The arc terrane is characterized by two temporally and petrologically distinct suites: an older intraoceanic suite and a younger Andean margin suite (Dunphy & Ludden, 1998). The older suite includes calc-alkaline diorite–tonalite gneiss, basaltic andesite, and rhyolite, and is dated between 1863 ± 2 and 1845 ± 2 Ma (Fig. 3; St-Onge *et al.*, 1992; Machado *et al.*, 1993; R. R. Parrish, unpublished data). The younger suite comprises crosscutting monzodiorite to granite plutons and is bracketed between $1842 +5/-3$ and $1820 +4/-3$ Ma (Fig. 3; Parrish, 1989, unpublished data; Machado *et al.*, 1993; Scott, 1997; Scott & Wodicka, 1998).

Downloaded from http://petrology.oxfordjournals.org/ by guest on June 7, 2013



Fig. 1. Summary geological map of North America, modified from Hoffman (1988). The map shows the extent of the Paleoproterozoic Trans-Hudson Orogen, the location of the bounding upper-plate Wyoming, Hearne, Rae, Slave, and North Atlantic cratons and lower-plate Superior craton of Archean age, and the extent of post-1·8 Ga North American cover.

Microcontinent and granite batholith

On southern Baffin Island, a second south-verging crustal suture (Soper River suture, Figs 2 and 4c; St-Onge *et al.*, 2001) separates the Narsajuaq arc in its footwall from Archean and Paleoproterozoic units of the Meta Incognita microcontinent (St-Onge *et al.*, 2000a) in its hanging wall. The microcontinent comprises (Figs 2 and 4): (1) a clastic–carbonate shelf succession (Lake Harbour Group) and its crystalline basement; (2) an overlying foreland basin succession (Blandford Bay assemblage); (3) an extensive suite of quartz diorite to monzogranitic plutons (Cumberland batholith) that intrude both the platformal and foreland basin rocks and underlying crystalline basement. The age of the shelf succession and foreland basin is bracketed between 1934 ± 2 and *ca.* 1880 Ma (Fig. 3; Scott, 1997, unpublished data; Scott *et al.*, 2002). Orthogneisses from the stratigraphic basement to the Lake Harbour Group have yielded Archean ages between 3019 ± 5 and 2784 ± 9 Ma (Scott, 1998, 1999) and a Paleoproterozoic age of $1950 + 6/-4$ Ma (Scott & Wodicka, 1998), whereas plutons of the Cumberland batholith have yielded ages between $1865 + 4/-2$ and 1848 ± 2 Ma (Jackson *et al.*, 1990; Wodicka & Scott, 1997; Scott & Wodicka, 1998; Scott, 1999) (Fig. 3).

Upper-plate cratonic margin

In the central Baffin Island area (top part of island shown in Fig. 2) felsic orthogneisses, metamorphosed supracrustal rocks, and younger felsic plutonic rocks range in age between $2868 + 13/-12$ and 2702 ± 3 Ma (Fig. 3; Jackson, 2000; Wodicka *et al.*, 2002b; Bethune & Scammel, 2003; D. J. Scott, unpublished data; N. Wodicka, unpublished data) and belong to the upper-plate Rae craton (Jackson, 1969, 2000; Bethune & Scammell, 2003; Scott *et al.*, 2003). The southern margin of the craton is unconformably overlain by the Paleoproterozoic Piling

Downloaded from http://petrology.oxfordjournals.org/ by guest on June 7, 2013

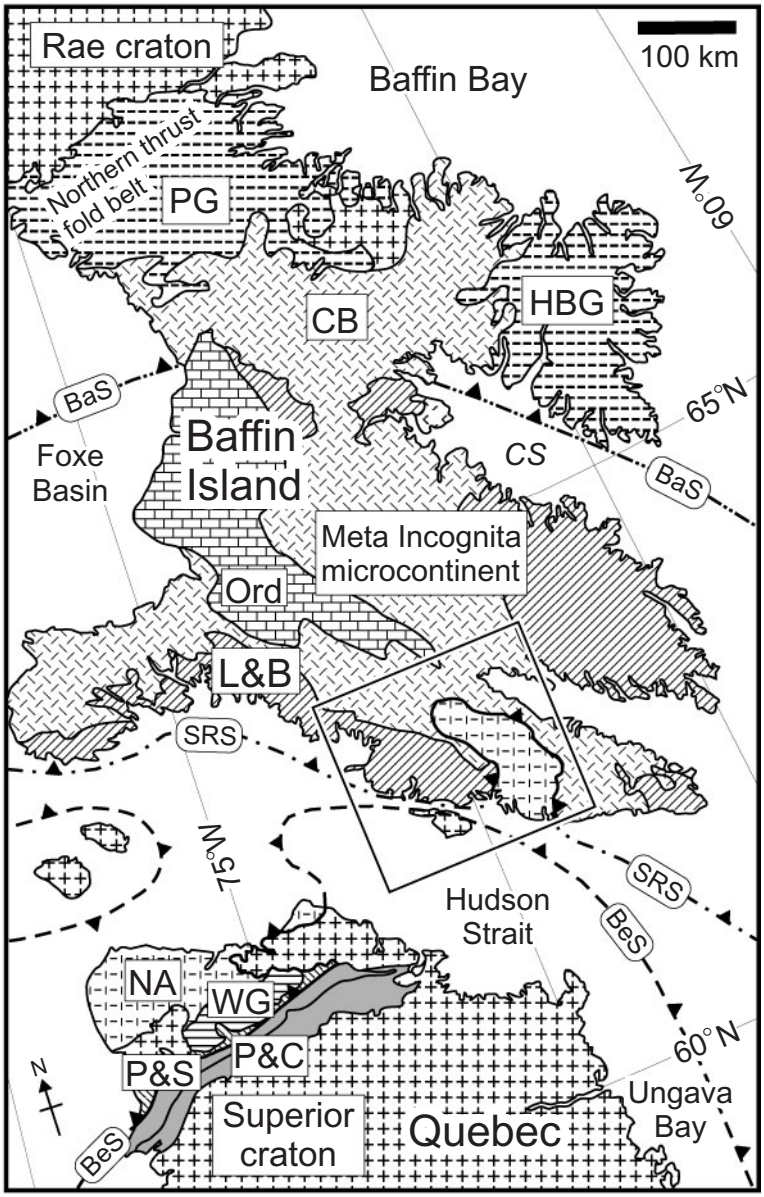


Fig. 2. Simplified geological map of the Quebec–Baffin segment of the Trans-Hudson Orogen. The map provides the regional tectonic context for the southern Baffin Island study area (outlined with the black rectangle and shown in greater detail in Fig. 5). Principal tectonostratigraphic units and bounding crustal sutures are described in the text. BaS, Baffin suture; BeS, Bergeron suture; CB, Cumberland batholith; CS, Cumberland Sound; HBG, Hoare Bay Group; L&B, Lake Harbour Group and Blandford Bay assemblage; NA, Narsajuaq arc; Ord, Ordovician cover; P&S, Parent and Spartan groups; P&C, Povungnituk and Chukotat groups; PG, Piling Group; SRS, Soper River suture; WG, Watts Group.

Group (Scott *et al.*, 2003; and references therein; Figs 2 and 4a), which comprises rift, shelf margin, and foredeep strata ranging in age between 2159 ± 16 Ma and 1897 + 7/–4 Ma (Fig. 3; Wodicka *et al.*, 2002b; N. Wodicka, unpublished data). Various felsic plutonic rocks, ranging in age from 1·90 to 1·85 Ga (Fig. 3) and including the northernmost component of the Cumberland batholith (Wodicka *et al.*, 2002*b*), intrude the Piling Group. Accretion of the Meta Incognita microcontinent to the southern margin of the Rae craton is proposed by St-Onge *et al.* (2005*a*) to have occurred across the Baffin suture (BaS; Fig. 3) between *ca.* 1880 and 1865 Ma, with the trace of the early suture tentatively situated at the head of Cumberland Sound (Fig. 2).

Downloaded from http://petrology.oxfordjournals.org/ by guest on June 7, 2013

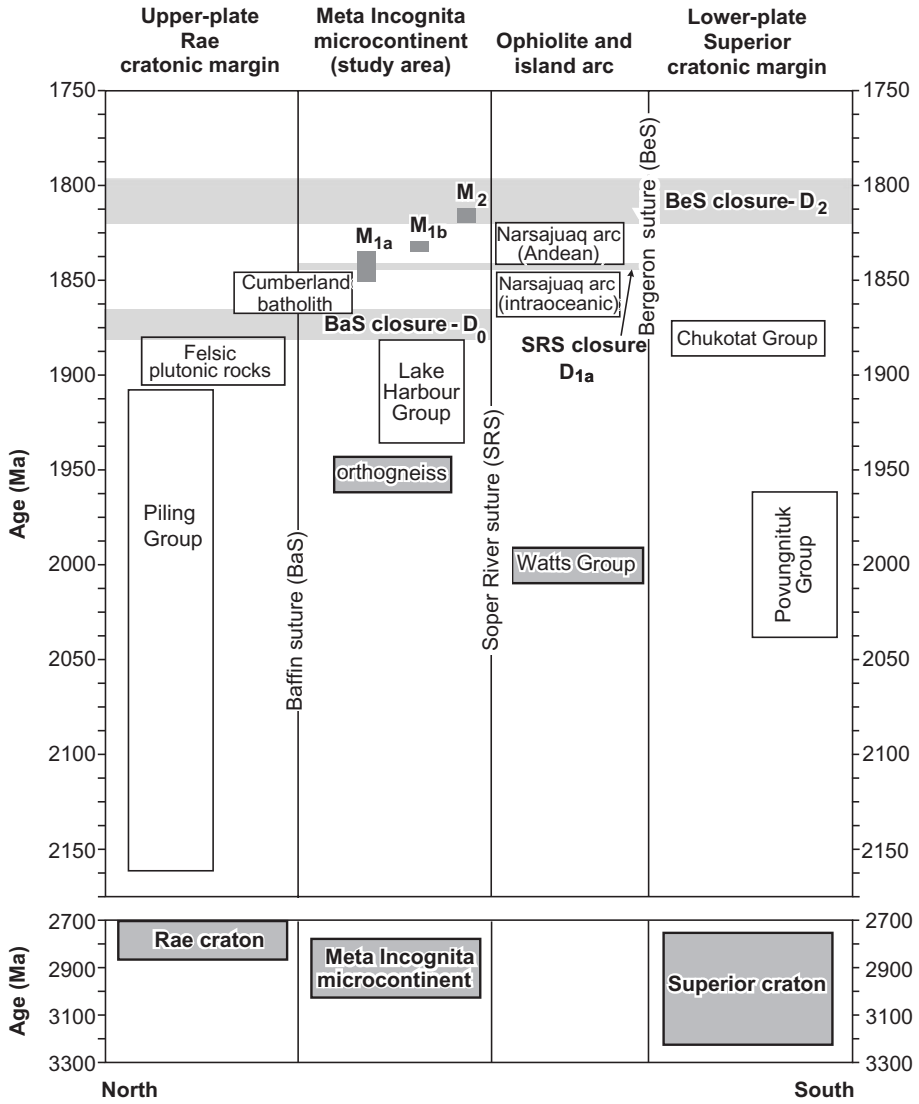


Fig. 3. Tectonic summary diagram for the Quebec–Baffin segment of the Trans-Hudson Orogen. The diagram documents the time intervals associated with the accumulation and emplacement of principal tectonostratigraphic and plutonic units in the study area and adjacent tectonic domains. Rectangles with a darker shade correspond to (Archean or Paleoproterozoic) basement units, open rectangles identify Paleoproterozoic supracrustal groups and magmatic suites, and shaded horizontal bars (D_0–D_2) identify the extent and age of bounding crustal sutures. M_{1a}–M_2 are the regional metamorphic events documented in the southern Baffin Island study area. (See text for sources of data and description.)

TECTONIC EVENTS, DEFORMATION FABRICS, AND METAMORPHIC ASSEMBLAGES, SOUTHERN BAFFIN ISLAND

Integrated tectonostratigraphic, structural and petrological fieldwork in the southern Baffin Island region has led to the recognition of a number of regional tectonothermal events of Paleoproterozoic age. These are schematically illustrated in Fig. 4 and an overview of the salient features of each event, and consequent development of deformation fabrics and metamorphic assemblages as documented in the study area are presented below.

D_0: accretion of Meta Incognita microcontinent

Map-scale D_0 tectonic contacts, which imbricate basement and cover units within the study area (Fig. 5), post-date deposition of the supracrustal units of the Lake Harbour Group and pre-date emplacement of the Cumberland batholith (St-Onge *et al.*, 1999*b*). The repetition of units by D_0 structures is suggestive of thrust imbrication,

Downloaded from http://petrology.oxfordjournals.org/ by guest on June 7, 2013

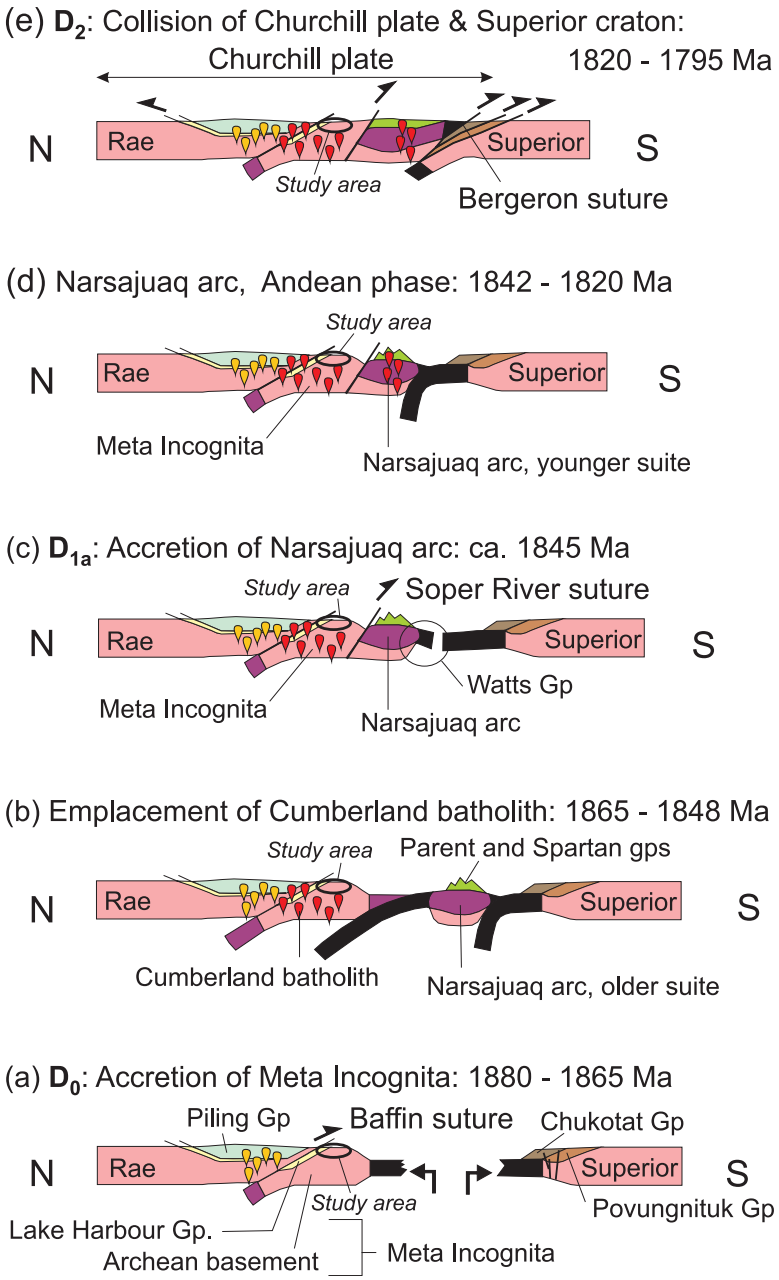


Fig. 4. Schematic cross-sections illustrating the regional tectonic evolution of the Quebec–Baffin Island segment of the Trans-Hudson Orogen for the period 1880–1795 Ma based on work presented by St-Onge *et al.* (1992, 1999*a*, 2001, 2002) and Scott *et al.* (2003): (a) accretion of the Meta Incognita microcontinent and its cover sequence (Lake Harbour Group) to the northern Rae craton and its cover sequence (Piling Group) with closure of the Baffin suture (BaS on Fig. 3) at *ca.* 1880–1865 Ma. Yellow polygons refer to the plutons that pre-date microcontinent accretion and are dated at *ca.* 1895 Ma (Jackson, 2002; St-Onge *et al.*, 2005*b*). The Povungnituk and Chukotat groups demarcate the northern rift margin of the Superior craton; (b) emplacement of the Cumberland batholith (red polygons) into the leading edge of the composite Churchill plate *ca.* 1865–1848 Ma. Accumulation of the Parent and Spartan groups in an intra-oceanic setting (Narsajuaq arc, older suite) above a second north-dipping subduction zone; (c) accretion of the Narsajuaq arc to the composite Churchill plate and formation of the Soper River suture (SRS on Fig. 3) at *ca.* 1845 Ma; (d) Andean phase of the Narsajuaq arc (younger suite) above a north-dipping subduction zone *ca.* 1842–1820 Ma; (e) terminal collision of the composite Churchill plate with the lower-plate Superior craton and closure of the Bergeron suture (BeS on Fig. 3) at *ca.* 1820–1795 Ma with reactivation of upper-plate domains. References for age determinations are given in the text. The relative position of the southern Baffin Island study area is shown for each time interval. Black fill in all cross-sections represents oceanic crust.

Downloaded from http://petrology.oxfordjournals.org/ by guest on June 7, 2013

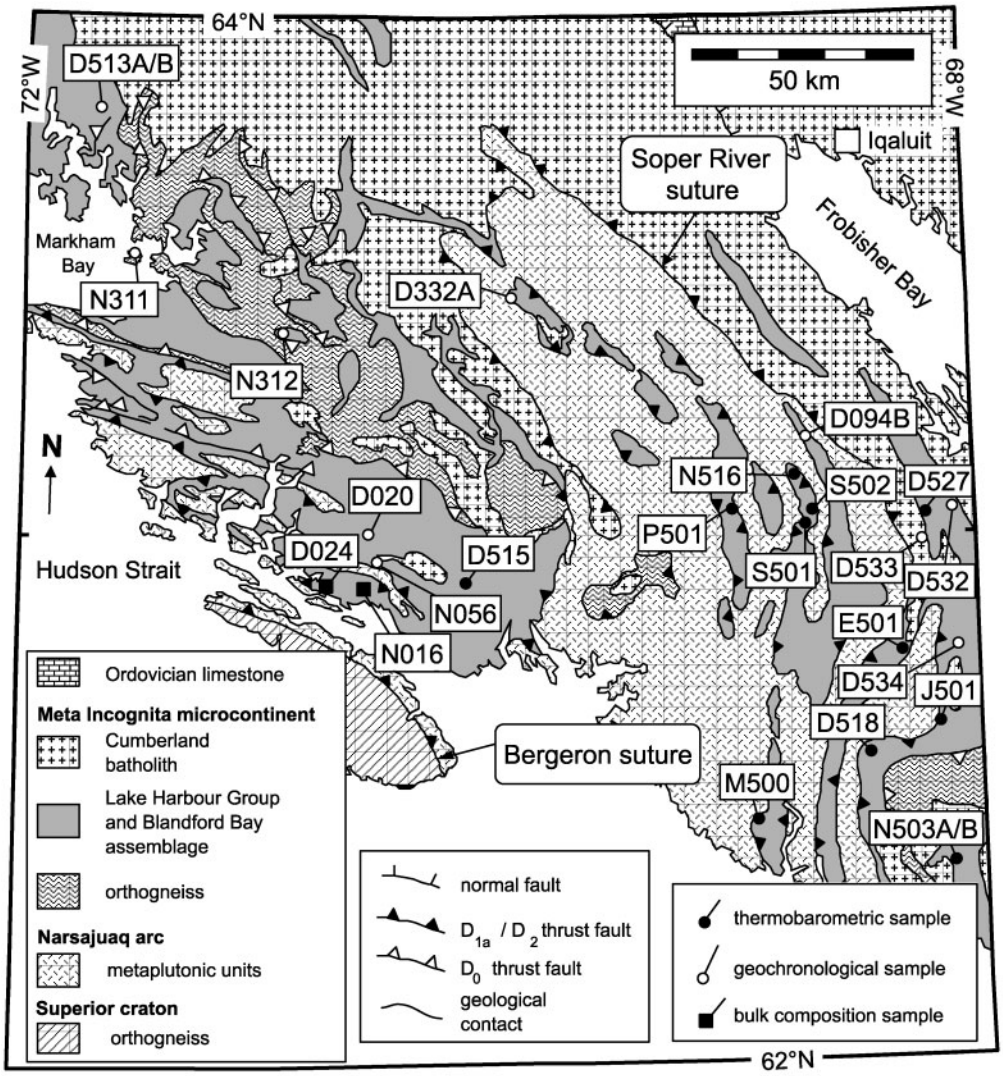


Fig. 5. Geological map of southern Baffin Island modified from St-Onge *et al.* (1999b) showing the distribution of samples in the study area. Principal tectonic elements and crustal sutures are discussed in the text. The location of samples used for thermobarometry (D515, D518, D527, E501, J501, M500, N503A/B, N516, P501, S501, S502), phase diagram calculation (D024, N016) and geochronology (D020, D094B, D332A, D513A/B, D532, D533, D534, N056, N311, N312, S502) is indicated.

but the direction, geometry, and magnitude of early displacements in southern Baffin Island are not known. The D_0 structures are interpreted as resulting from the accretion of the Meta-Incognita microcontinent to the southern Rae margin (Fig. 4a) and closing of the Baffin suture (BaS; Fig. 3). In the study area, mesoscopic and microscopic deformation fabrics and mineral assemblages potentially associated with the D_0 structures are not preserved, because of the pervasive recrystallization and foliation development that occurred during the subsequent prograde D_{1a}–M_{1a} event (see below).

D_{1a}: accretion of Narsajuaq arc

Continued convergence between the southern margin of the accreted Meta Incognita microcontinent and crustal domains to the south led to D_{1a} accretion of the Narsajuaq arc (Fig. 4c) and formation of the Soper River suture (Fig. 2). Closing of the suture (SRS; Fig. 3) is bracketed between 1845 ± 2 Ma, the age of the youngest unit associated with the intra-oceanic phase of Narsajuaq arc (Dunphy & Ludden, 1998) and $1842 + 5/-3$ Ma (Scott, 1997), the age of the oldest plutonic unit of the Andean-margin phase of the Narsajuaq arc.

The Soper River suture marks the structural base of the Meta Incognita microcontinent. Deformation in the suture's footwall includes: (1) structural repetitions and truncations of distinct tectonostratigraphic units yielding an overall SW-verging ramp–flat fault geometry (Scott *et al.*, 1997); (2) development of ribbon mylonites; and (3) transposition of crosscutting intrusive units into

Downloaded from http://petrology.oxfordjournals.org/ by guest on June 7, 2013

parallelism with the suture. Deformation in the hanging wall is both extensive and penetrative, with D_{1a} manifest as a regional syn-metamorphic foliation (S_{1a}; see below) that affects all pre- to syn-accretion units within the microcontinent terrane.

M_{1a}: prograde granulite-facies metamorphism, Meta Incognita microcontinent

The M_{1a} metamorphism of southern Baffin Island is characterized by pelitic and psammitic units of the Lake Harbour Group generally containing subsets of the granulite-facies assemblage garnet–cordierite–sillimanite–biotite–plagioclase–K-feldspar–quartz–melt (here and elsewhere interpreted from granitic leucosome) (Fig. 6a) and mafic units containing subsets of the assemblage garnet–orthopyroxene–clinopyroxene–hornblende–biotite–plagioclase (Fig. 7a).

At the macroscopic and microscopic scale, the distribution of these assemblages is strongly domainal and associated with the development of a pervasive millimetre- to centimetre-scale compositional foliation (S_{1a}; Fig. 6a). In metapelitic units, S_{1a} is defined by layers of coarse (2 cm × 1 cm) subhedral garnet, abundant (2–3 mm) euhedral sillimanite, (1–2 mm) biotite, and (4 mm × 1·5 mm) anhedral cordierite (plus quartz and plagioclase), alternating with layers of dominantly plagioclase, K-feldspar, and quartz. The S_{1a} foliation is further enhanced by the alignment of biotite, sillimanite, and elongate grains of garnet and cordierite (Fig. 6a). Both garnet and cordierite are strongly poikiloblastic, containing abundant sub-millimetre scale inclusions of sillimanite generally aligned parallel to the dominant S_{1a} foliation. Overall, garnet and sillimanite dominate the S_{1a} foliation, suggesting that these phases were principal products of the M_{1a} event, whereas cordierite, although almost always present, is notably less abundant. In the samples selected

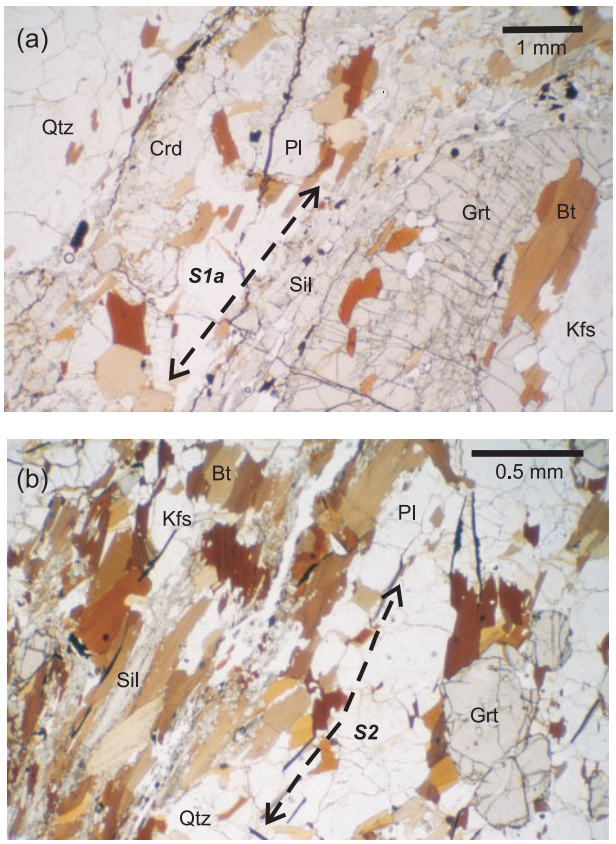


Fig. 6. (a) S_{1a} granulite-facies garnet–cordierite–sillimanite–biotite–plagioclase–quartz–K-feldspar–melt assemblage in metapelite (sample D515). Note well-developed syn-metamorphic S_{1a} compositional layering. Sample location shown in Fig. 5. (b) Retrograde S_2 garnet–sillimanite–biotite–plagioclase–quartz–K-feldspar (plus cordierite and melt) assemblage in metapelite (sample D518). Note small sub-equant S_2 garnet porphyroblasts cross-cutting the S_2 biotite foliation. Sample location shown in Fig. 5.

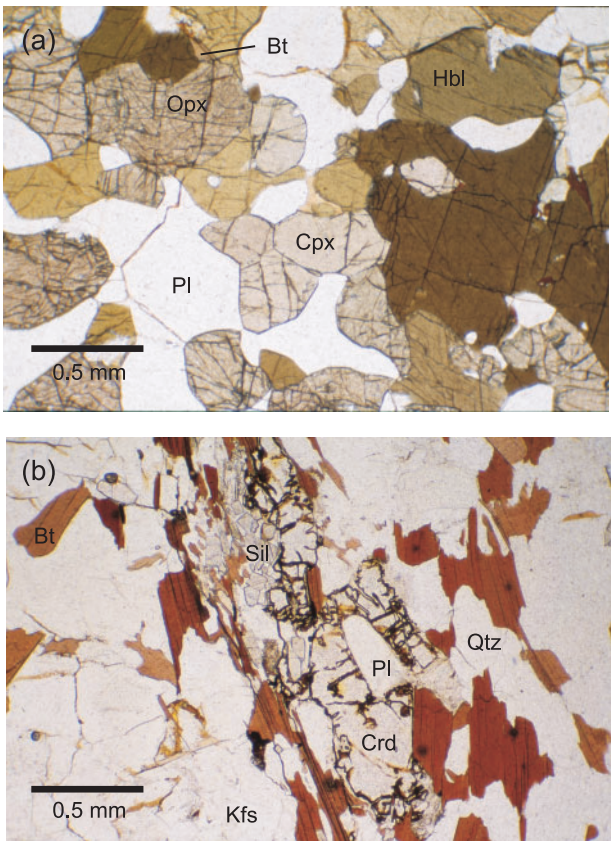


Fig. 7. (a) M_{1a} granulite-facies orthopyroxene–clinopyroxene–hornblende–biotite–plagioclase (plus garnet) assemblage in mafic sill (sample N503A). Sample location shown in Fig. 5. (b) S_{1a} cordierite in metapelite (sample D515). (Note the recessive and embayed morphology of the cordierite, indicating a lack of textural equilibrium between the cordierite and adjacent mineral phases.) Sample location shown in Fig. 5.

Downloaded from http://petrology.oxfordjournals.org/ by guest on June 7, 2013

for this study, all of these minerals are unaltered and found in mutual contact, thus appearing to be in textural equilibrium, with the exception of S_{1a} cordierite (Fig. 7b). This mineral generally presents a marked recessive or embayed morphology with adjacent garnet, biotite and/or sillimanite within the S_{1a} foliation, which suggests a (late?) stage of disequilibria during the M_{1a} thermal event.

Within the study area, the granulite-facies foliation is generally shallow-dipping (<45°), invariably parallel to lithological contacts between supracrustal units (St-Onge *et al.*, 1999b) and, in metasedimentary units, is interpreted as a metamorphic enhancement of primary bedding (S_0). Mafic units are generally massive, although locally S_{1a} is defined by the alternating distribution of dominantly ferromagnesian-rich layers (comprising 1–1·5 cm scale garnet porphyroblasts, and granoblastic millimetre-scale orthopyroxene, clinopyroxene, hornblende, and biotite grains; Fig. 7a) and layers comprising dominantly plagioclase. The alignment of hornblende and biotite also highlights the S_{1a} foliation when present. Garnet porphyroblasts are generally poikiloblastic and contain inclusions of all the other S_{1a} phases (plagioclase, orthopyroxene, clinopyroxene, hornblende, and biotite), suggesting equilibrium growth during M_{1a}.

M_{1b}: high-*T* thermal perturbation, Meta Incognita microcontinent

Concordant U–Pb ages from metamorphic monazite and zircon in siliciclastic and gneiss samples (Scott & Gauthier, 1996; Wodicka & Scott, 1997; Scott & Wodicka, 1998; this study) suggest that rocks from the study area experienced a thermal perturbation at *ca.* 1833–1829 Ma. As discussed below, these ages may represent a distinct thermal event (here termed M_{1b}) related to emplacement of *ca.* 1834–1831 Ma felsic dykes and plugs. However, other than the growth of monazite and zircon, as well as orthopyroxene in some of the more mafic plugs, no other metamorphic mineral phase or regional foliation development is documented for M_{1b}. Whether M_{1b} is a distinct thermal pulse or part of a protracted M_1 metamorphic event is discussed further after presentation of the geochronological data from the southern Baffin Island study area.

D_2: collision of the northern (Churchill) plate and the Superior craton

The D_2 collision of the northern (Churchill) plate (i.e. Rae craton plus accreted microcontinent, arc, and ophiolitic units described above) with the Superior craton involved: (1) closure of the Bergeron suture (Figs 2 and 4e) and formation of a foreland thrust–fold belt within the lower-plate Superior domain (Fig. 4e; Lucas, 1989; St-Onge *et al.*, 2001); (2) imbrication of tectonostratigraphic units on southern Baffin Island including reactivation and further shortening across the Soper River suture; and (3) D_2–M_2 modification of pre-existing fabrics in the study area (see below). Terminal collision across the Bergeron suture (BeS; Fig. 3) is bracketed between 1820 +4/–3 Ma, the age of the youngest dated plutonic unit in the hanging wall of the suture (Scott & Wodicka, 1998) and 1795 ± 2 Ma, the age of a post-collisional syenogranitic dyke that crosscuts the suture on southern Baffin Island (Wodicka & Scott, 1997).

Within the hanging wall of the Bergeron suture on southern Baffin Island, principal modifications to pre-existing fabrics during D_2 include the development of a more finely layered S_2 foliation in metasedimentary units (see below) and the transposition of angular compositional discordances in metaplutonic rocks. Local reactivation of the Soper River suture is manifest by outcrop- to map-scale recumbent folding of earlier (S_{1a}) foliations (St-Onge et al., 1999*b*).

M_2: retrograde amphibolite-facies metamorphism, Meta Incognita microcontinent

D_2 collisional deformation is associated with prograde greenschist- to amphibolite-facies metamorphism of the lower-plate Superior cratonic margin and retrograde upper amphibolite-facies metamorphism of the granulites of southern Baffin Island (St-Onge *et al.*, 2000*b*).

Zones of D_2 deformation within psammitic and pelitic units in the study area are marked by the pervasive growth of S_2 biotite–sillimanite–quartz ± garnet ± cordierite at the expense of the S_{1a} garnet–cordierite assemblages described above. Abundant, small, S_2 biotite (0·3–0·5 mm) and sillimanite (0·1–0·5 mm) laths define a distinct, penetrative, schistose (finely layered), sub-millimetre-scale foliation (Fig. 6b). Sparse, small, sub-equant (0·5–1·0 mm) euhedral to slightly ellipsoid subhedral grains of garnet are generally aligned with and overgrow the biotite–sillimanite foliation (Fig. 6b). Based on the relationship with the S_2 foliation, these grains are interpreted as M_2 in age. Their size and shape, and the fact that they overgrow the S_2 foliation, make them readily distinguishable from the larger, elongate and more voluminous S_{1a} garnets (Fig. 6a). Within zones of D_2 deformation, the S_{1a} garnets (when present) are wrapped by (and thus pre-date) the S_2 foliation and display embayed, corroded outlines. Cordierite is either absent, or present as sub-millimetre grains aligned in the S_2 foliation. As with garnet, the size and relationship of the S_2 cordierite grains to the foliation allows S_2 cordierite to be distinguished from S_{1a} cordierite. In some thin sections, the S_2 garnets are further mantled by a sub-millimetre rim of cordierite, suggesting late-stage replacement. New growth and recrystallization of zircon and monazite in metasedimentary units indicates that M_2 retrograde metamorphism occurred at *ca.* 1820 ± 1 to 1813 ± 2 Ma (Wodicka & Scott, 1997; Scott *et al.*, 2002; this study).

Downloaded from http://petrology.oxfordjournals.org/ by guest on June 7, 2013

Table 1: Mineral assemblages

Sample no.	Lithology	Foliation	Mineral assemblage
S_{1a} granulite-facies assemblage			
D515	pelite	well-developed S_{1a}	Grt–Crd–Sil–Bt–Pl–Kfs–Qtz–melt
S502	pelite	well-developed S_{1a}	Grt–Sil–Bt–Pl–Kfs–Qtz–melt
N503A	mafic sill	weakly developed S_{1a}	Opx–Cpx–Grt–Hbl–Bt–Pl
N503B	mafic sill	weakly developed S_{1a}	Opx–Cpx–Grt–Hbl–Bt–Pl
S_2 amphibolite-facies assemblage			
D518	pelite	pervasive S_2	Sil–Bt–Pl–Qtz–Kfs–Grt–Crd–melt
D527	pelite	pervasive S_2	Sil–Bt–Pl–Qtz–Kfs–Grt–melt
E501	pelite	pervasive S_2	Sil–Bt–Pl–Qtz–Kfs–Grt–melt
J501	pelite	pervasive S_2	Sil–Bt–Pl–Qtz–Kfs–Grt–Crd–melt
N516	pelite	pervasive S_2	Sil–Bt–Pl–Qtz–Kfs–Grt–Crd–melt
S_{1a} granulite facies-assemblage overprinted by S_2 amphibolite-facies assemblage			
M500	pelite	well-developed S_{1a} and moderate S_2 overprint	Sil–Bt–Pl–Qtz–Kfs–Grt–Crd–melt
P501	pelite	well-developed S_{1a} and moderate S_2 overprint	Sil–Bt–Pl–Qtz–Kfs–Grt–Crd–melt
S501	pelite	well-developed S_{1a} and moderate S_2 overprint	Sil–Bt–Pl–Qtz–Kfs–Grt–Crd–melt

Mineral abbreviations are after Kretz (1983).

METHODS

A suite of 25 samples was collected (Fig. 5) for an integrated structural–petrological–geochronological study of supracrustal rocks from the Meta Incognita microcontinent. Of these, 14 samples were utilized for textural observations, thermobarometric data, and phase diagram construction, whereas 12 samples were employed for U–Pb geochronological analysis of zircon, monazite, and titanite.

Thermobarometry

Samples of pelitic and mafic units from the Lake Harbour Group containing S_{1a} granulite-facies assemblages or S_2 amphibolite-facies assemblages (Table 1) appropriate for thermobarometric work were selected for analysis. Sample locations are given in Fig. 5. The spot-analyses were obtained at the Geological Survey of Canada (GSC) using a Cameca microbeam electron microprobe equipped with four wavelength-dispersive spectrometers and automated to produce simultaneous multi-element analyses and data reduction (Pouchou & Pichoir, 1984). Operating conditions were 15 kV accelerating voltage, specimen current of 10–30 nA and a counting time of 30 s. Standards used were appropriate minerals, oxides, and metals. A 10 μm beam spot was used for biotite and plagioclase and a more focused beam (*ca.* 3 μm) for garnet, cordierite, orthopyroxene, and clinopyroxene.

All ferromagnesian minerals and plagioclase grains were analysed along rim–core–rim traverses at regular intervals (0·02–0·25 mm depending on size, yielding on average 5–10 spot-analyses per traverse) to check for compositional zoning or heterogeneities. For each mineral grain, the identification of relatively homogeneous core and rim domains was followed by 5–7 spot-analyses per domain. These analyses were then averaged to provide a statistically robust dataset for the thermobarometric calculations. For any given sample, detailed analytical work focused on a part of the thin section (*ca.* 2–5 mm radius), which was judged to be optimal in terms of mutual mineral textural equilibrium and lack of alteration (with the exception of cordierite; see below), and contained within a single S_{1a} compositional layer or S_2 domain. Reconnaissance microprobing of mineral phases outside the areas of detailed analysis confirmed the compositional homogeneity of the mineral phases within any given compositional layer or domain for this suite of rocks. Within each area of detailed analytical work, the analysed minerals were selected so as to be separated from each other by one or two grains (distance of *ca.* 1 mm) that did not participate in the equilibrium of interest (for example, quartz or plagioclase in the case of analysed ferromagnesian minerals), to avoid potential local retrograde re-equilibration between minerals actually in contact (St-Onge, 1984, and references therein). Representative analyses (each an average of 5–7 spot-analyses) of orthopyroxene, clinopyroxene, garnet, cordierite, plagioclase, and biotite for the 12 thermobarometric samples are given in Tables 2–6.

Compositional zoning (see Spear, 1993; and references therein) is absent from most mineral phases analysed with

Downloaded from http://petrology.oxfordjournals.org/ by guest on June 7, 2013

Table 2: Ortho- and clinopyroxene analyses

	N503AR	N503BR	N503AR	N503BR
SiO_2	49·02	48·29	49·55	49·56
Al_2O_3	0·92	0·94	2·19	1·83
Fe_2O_3	1·79	2·77	2·87	4·00
TiO_2	0·02	0·07	0·30	0·17
Cr_2O_3	0·00	0·01	0·09	0·03
MgO	13·91	13·94	10·32	10·65
FeO	31·97	31·73	11·96	10·57
MnO	0·50	0·48	0·20	0·17
CaO	0·81	0·66	21·37	21·88
Na_2O	0·05	0·00	0·36	0·32
Total	98·99	98·89	99·21	99·18
Cations normalized to 6 oxygens				
Si	1·95	1·93	1·91	1·91
Al	0·04	0·04	0·10	0·08
Ti	0·00	0·00	0·01	0·01
Cr	0·00	0·00	0·00	0·00
Fe^{3+}	0·05	0·08	0·08	0·12
Fe^{2+}	1·07	1·06	0·39	0·34
Mn	0·02	0·02	0·01	0·01
Mg	0·83	0·83	0·59	0·61
Ca	0·04	0·03	0·88	0·90
Na	0·00	0·00	0·03	0·02
mg-no.	0·42	0·42	0·56	0·57
Wo	1·82	1·46	47·42	48·68
En	42·86	43·29	31·85	32·99
Fs	55·32	55·25	20·73	18·33
Event	M_{1a}	M_{1a}	M_{1a}	M_{1a}

Labels refer to samples; R, rim. *mg*-no. = Mg/(Mg + Fe^{2+} + Fe^{3+}). Fe^{3+} is derived from charge-balance calculation.

the exception of garnet. In S_{1a} samples D515 and S502 (Table 3) garnet is characterized by minor prograde compositional change from core to rim (increase in pyrope content, decrease in almandine and spessartine contents). In S_2 samples D518, J501 and N516, and samples M500, P501 and S501, which contain S_{1a} garnet cores and S_2 garnet rims (Table 3), garnet is characterized by a retrograde compositional change between core and rim (increase in calculated almandine and spessartine contents, decrease in pyrope content).

Pressure-temperature (P–T) estimates were calculated using the TWEEQU software (Berman, 1991) that incorporates the thermodynamic data of Berman (1988) together with revised data for garnet, cordierite, and biotite (Berman & Aranovich, 1996; TWQ version 2.02a; http://www.gis.nrcan.gc.ca/twq.html). The following independent set of equilibria were utilized for the P–T calculations:

In pelitic rocks:

$$\text{almandine} + \text{phlogopite} = \text{pyrope} + \text{annite} \quad (1)$$

$$3\,\text{cordierite} + 2\,\text{almandine} = +\,3\,\text{Fe} - \text{cordierite} + 2\,\text{pyrope} \quad (2)$$

$$\text{grossular} + \beta - \text{quartz} + 2\,\text{sillimanite} = 3\,\text{anorthite} \quad (3)$$

$$2\,\text{almandine} + 5\,\beta - \text{quartz} + 4\,\text{sillimanite} = 3\,\text{Fe} - \text{cordierite}. \quad (4)$$

In mafic rocks:

$$\text{almandine} + \text{phlogopite} = \text{pyrope} + \text{annite} \quad (1)$$

$$\text{almandine} = \text{corundum} + 3\,\text{ferrosilite} \quad (5)$$

$$\text{almandine} + 3\,\text{enstatite} = \text{pyrope} + 3\,\text{ferrosilite} \quad (6)$$

$$2\,\text{almandine} + \text{grossular} + 3\,\beta - \text{quartz} = 6\,\text{ferrosilite} + 3\,\text{anorthite} \quad (7)$$

$$\text{almandine} + 3\,\text{diopside} = \text{pyrope} + 3\,\text{hedenbergite} \quad (8)$$

$$\text{almandine} + 2\,\text{grossular} + 3\,\beta - \text{quartz} = 3\,\text{hedenbergite} + 3\,\text{anorthite}. \quad (9)$$

Equilibria (3), (4), (7), and (9) serve as barometers and equilibria (1), (2), (5), (6), and (8) serve as thermometers. Absolute errors on the thermobarometric results are considered to be *ca.* ±50°C and 1 kbar [see Essene, 1989; Berman, 1991; see also St-Onge & Ijewliw (1996) for discussion]. For the samples discussed in the text, we also report one standard deviation errors for the TWEEQU equilibria intersections, as computed by Berman's (1991) INTERSX program. The INTERSX standard deviations allow an assessment of the overall consistency of the results, but do not represent statistically valid uncertainties (Berman, 1991). Finally, given that a same set of equilibria is used for the thermobarometric calculations of all the pelitic assemblages [equilibria (1)–(4) above] and another same set of equilibria for the mafic assemblages [equilibria (1), (5)–(9) above], the calculations of relative changes in recorded P–T conditions between and within either pelitic or mafic samples (see below) should be reliable, as relative thermobarometry with the same set of equilibria depends dominantly on changes in the compositional part of ln κ terms.

Phase diagram calculations

The program DOMINO (De Capitani, 1994; http://titan.minpet.unibas.ch/minpet/groups/theriak/theruser.html, August, 2003 version) and the thermodynamic dataset

Downloaded from http://petrology.oxfordjournals.org/ by guest on June 7, 2013

Table 3: Garnet analyses

	D515C	D515R	S502C	S502R	N503AR	N503BR	D518C	D518R	D527C	D527R	E501C	E501R	J501C	J501R	N516C	N516R	M500C	M500R	P501C	P501R	S501C	S501R
SiO_2	38·62	37·65	39·19	38·32	37·58	38·01	37·00	36·94	38·81	38·81	37·41	38·99	38·53	37·87	37·74	37·68	39·99	39·39	38·61	38·16	38·58	37·37
TiO_2	0·08	0·01	0·00	0·07	0·16	0·00	0·02	0·02	0·01	0·06	0·02	0·00	0·11	0·00	0·07	0·00	0·05	0·11	0·00	0·07	0·07	0·00
Al_2O_3	21·27	21·90	22·26	22·09	20·72	20·86	21·30	21·09	21·62	21·27	21·61	21·41	20·97	20·97	21·28	20·97	22·12	21·98	21·38	21·93	21·43	21·07
Cr_2O_3	0·07	0·02	0·08	0·03	0·04	0·05	0·03	0·08	0·05	0·00	0·00	0·02	0·04	0·15	0·03	0·03	0·17	0·29	0·07	0·14	0·02	0·09
Fe_2O_3	0·00	1·09	0·65	0·85	1·30	0·83	0·69	0·64	0·54	0·82	1·51	0·00	0·00	0·86	0·45	0·65	0·16	0·00	0·61	0·43	0·46	1·35
FeO	29·13	27·66	25·43	25·01	28·32	28·58	31·26	33·86	28·06	28·30	28·53	29·49	30·65	30·88	32·04	33·44	20·99	23·35	28·50	30·23	31·26	31·43
MgO	8·07	8·71	10·89	10·65	3·67	3·67	5·71	4·50	9·29	9·21	8·04	8·31	7·20	6·97	6·43	5·42	14·06	12·31	8·86	7·58	7·40	6·45
MnO	0·77	0·61	0·53	0·42	1·24	1·26	0·76	0·97	0·43	0·45	0·47	0·66	0·48	0·62	0·33	0·43	0·63	0·68	0·41	0·45	0·30	0·34
CaO	0·85	0·92	1·13	1·15	7·01	7·07	1·59	1·02	1·07	1·02	1·11	1·10	1·18	1·06	1·06	1·16	0·89	0·97	1·14	1·16	1·13	1·10
Total	98·86	98·57	100·16	98·59	100·04	100·33	98·36	99·12	99·88	99·94	98·70	99·98	99·16	99·38	99·43	99·78	99·06	99·08	99·58	100·15	100·65	99·20
Cations normalized to 24 oxygens																						
Si	6·06	5·91	5·96	5·93	5·96	6·00	5·94	5·95	6·00	6·01	5·90	6·05	6·07	5·99	5·98	5·99	6·02	6·00	6·00	5·95	6·00	5·94
Ti	0·01	0·00	0·00	0·01	0·02	0·00	0·00	0·00	0·00	0·01	0·00	0·00	0·01	0·00	0·01	0·00	0·01	0·01	0·00	0·01	0·01	0·00
Al	3·93	4·05	3·99	4·03	3·87	3·89	4·03	4·01	3·94	3·88	4·02	3·92	3·89	3·91	3·97	3·93	3·92	3·95	3·92	4·03	3·93	3·95
Cr	0·01	0·00	0·01	0·00	0·01	0·01	0·00	0·01	0·01	0·00	0·00	0·00	0·01	0·02	0·00	0·00	0·02	0·03	0·01	0·02	0·00	0·01
Fe^{2+}	3·82	3·63	3·24	3·23	3·76	3·78	4·20	4·56	3·63	3·66	3·76	3·83	4·04	4·08	4·24	4·45	2·64	2·97	3·71	3·94	4·07	4·18
Fe^{3+}	0·00	0·13	0·08	0·10	0·16	0·10	0·08	0·08	0·06	0·10	0·18	0·00	0·00	0·10	0·05	0·08	0·02	0·00	0·07	0·05	0·05	0·16
Mn	0·10	0·08	0·07	0·06	0·17	0·17	0·10	0·13	0·06	0·06	0·06	0·09	0·06	0·08	0·05	0·06	0·08	0·09	0·05	0·06	0·04	0·05
Mg	1·89	2·04	2·47	2·46	0·87	0·86	1·37	1·08	2·14	2·12	1·89	1·92	1·69	1·64	1·52	1·29	3·15	2·79	2·05	1·76	1·71	1·53
Ca	0·14	0·16	0·18	0·19	1·19	1·20	0·27	0·18	0·18	0·17	0·19	0·18	0·20	0·18	0·18	0·20	0·14	0·16	0·19	0·19	0·19	0·19
mg-no.	0·33	0·35	0·42	0·42	0·18	0·18	0·24	0·19	0·36	0·36	0·32	0·33	0·30	0·28	0·26	0·22	0·54	0·48	0·35	0·30	0·29	0·26
Pyrope	31·76	33·77	41·37	40·73	14·15	14·17	22·76	17·91	35·26	34·70	31·09	31·89	28·21	26·97	25·17	21·22	52·24	46·42	33·77	29·33	28·22	25·04
Almandine	64·20	60·10	54·27	53·48	61·14	62·27	69·77	75·62	59·80	59·90	61·84	63·62	67·45	67·11	70·20	73·19	43·78	49·42	61·12	65·67	67·16	68·41
Spessartine	1·68	1·32	1·17	0·99	2·76	2·80	1·66	2·16	0·99	0·98	0·99	1·50	1·00	1·32	0·83	0·99	1·33	1·50	0·82	1·00	0·66	0·82
Grossular	2·35	2·65	3·02	3·15	19·35	19·77	4·49	2·99	2·97	2·78	3·13	2·99	3·34	2·96	2·98	3·29	2·32	2·66	3·13	3·17	3·14	3·11
Event	M_{1a}	M_{1a}	M_{1a}	M_{1a}	M_{1a}	M_{1a}	M_2	M_2	M_2	M_2	M_2	M_2	M_2	M_2	M_2	M_2	M_{1a}	M_2	M_{1a}	M_2	M_{1a}	M_2

Labels refer to samples; C, core; R, rim. *mg*-no. $=Mg/(Mg+Fe^{2+}+Fe^{3+})$. Fe^{3+} is derived from charge-balance calculation.

Downloaded from http://petrology.oxfordjournals.org/ by guest on June 7, 2013

Table 4: Cordierite analyses

	D515C	D515R	D518C	D518R	J501C	J501R	N516C	N516R	M500C	M500R	P501C	P501R	S501C	S501R
SiO_2	47·10	47·52	48·20	47·70	48·19	48·24	49·02	47·93	47·85	48·26	47·29	47·58	49·31	49·42
Al_2O_3	33·38	33·56	33·02	33·28	33·55	33·73	32·90	33·19	33·05	33·23	33·53	33·19	33·04	32·76
TiO_2	0·02	0·00	0·03	0·02	0·05	0·06	0·03	0·00	0·00	0·00	0·00	0·00	0·01	0·03
Fe_2O_3	2·00	1·93	0·42	1·64	1·36	2·00	0·09	2·07	2·65	1·99	1·84	1·55	0·00	0·00
FeO	4·10	4·47	6·79	6·06	4·74	4·44	7·40	5·80	0·86	1·43	4·43	4·48	7·02	6·93
MgO	9·62	9·56	8·74	8·98	9·92	9·97	9·04	9·08	11·59	11·63	9·60	9·74	9·18	9·30
MnO	0·05	0·02	0·10	0·01	0·08	0·05	0·02	0·04	0·07	0·03	0·07	0·04	0·04	0·03
Na_2O	0·11	0·10	0·09	0·02	0·02	0·02	0·00	0·07	0·12	0·07	0·03	0·06	0·00	0·00
CaO	0·02	0·02	0·02	0·02	0·00	0·01	0·05	0·02	0·03	0·03	0·01	0·01	0·03	0·00
K_2O	0·00	0·01	0·02	0·02	0·00	0·02	0·00	0·01	0·01	0·00	0·00	0·01	0·00	0·00
Total	96·40	97·19	97·43	97·75	97·91	98·54	98·55	98·21	96·23	96·67	96·80	96·66	98·63	98·47
Cations normalized to 18 oxygens														
Si	4·89	4·90	4·98	4·92	4·93	4·90	5·01	4·92	4·91	4·93	4·89	4·92	5·02	5·04
Al	4·08	4·08	4·02	4·04	4·04	4·04	3·96	4·02	4·00	4·00	4·09	4·05	3·97	3·94
Ti	0·00	0·00	0·00	0·00	0·00	0·00	0·00	0·00	0·00	0·00	0·00	0·00	0·00	0·00
Fe^{3+}	0·16	0·15	0·03	0·13	0·10	0·15	0·01	0·16	0·21	0·15	0·14	0·12	0·00	0·00
Fe^{2+}	0·36	0·39	0·59	0·52	0·41	0·38	0·63	0·50	0·07	0·12	0·38	0·39	0·60	0·59
Mg	1·49	1·47	1·35	1·38	1·51	1·51	1·38	1·39	1·77	1·77	1·48	1·50	1·39	1·41
Mn	0·00	0·00	0·01	0·00	0·01	0·00	0·00	0·00	0·01	0·00	0·01	0·00	0·00	0·00
Na	0·02	0·02	0·02	0·00	0·00	0·00	0·00	0·01	0·02	0·01	0·01	0·01	0·00	0·00
Ca	0·00	0·00	0·00	0·00	0·00	0·00	0·01	0·00	0·00	0·00	0·00	0·00	0·00	0·00
K	0·00	0·00	0·00	0·00	0·00	0·00	0·00	0·00	0·00	0·00	0·00	0·00	0·00	0·00
mg-no.	0·74	0·73	0·68	0·68	0·75	0·74	0·68	0·68	0·86	0·87	0·74	0·75	0·70	0·71
Event	M_{1a}	M_{1a}	M_2	M_2	M_2	M_2	M_2	M_2	M_{1a}	M_2	M_{1a}	M_2	M_{1a}	M_2

Labels refer to samples; C, core; R, rim. *mg*-no. $=Mg/(Mg+Fe^{2+}+Fe^{3+})$. Fe^{3+} is derived from charge-balance calculation.

of Holland & Powell (1998) were used to calculate phase diagrams in the expanded pelitic model system $MnO–CaO–Na_2O–K_2O–FeO–MgO–Al_2O_3–SiO_2–H_2O$ (MnCNKFMASH; e.g. Spear, 1993; Tinkham *et al.*, 2003). The phases considered in the construction of the phase diagrams were orthopyroxene, garnet, cordierite, sillimanite, kyanite, andalusite, K-feldspar, plagioclase, quartz, biotite, muscovite, chlorite, staurolite, melt, and H_2O. Details and sources of the activity–composition models employed in this study have been given by Tinkham *et al.* (2003), with the biotite and chlorite models reparameterized for use with DOMINO (De Capitani, 2004, unpublished data). The H_2O content in the system was reduced approximately to the point that the assemblage was just saturated immediately subsolidus at 6 kbar, following the procedure reported by White *et al.* (2001).

The bulk-rock composition of a large (12 kg) unaltered sample of Lake Harbour Group metapelite (N016; Fig. 5) containing an S_{1a} garnet–cordierite–sillimanite–biotite–plagioclase–K-feldspar–quartz–melt assemblage, and characterized by regular millimetre-scale compositional layering, was obtained from X-ray fluorescence (XRF) analysis as reported by Thériault *et al.* (2001). Whole-rock XRF data for sample N016 are considered a reasonable proxy for bulk composition during M_{1a} regional metamorphism and porphyroblast growth in the study area based on the large size of the sample and the millimetre scale of the S_{1a} compositional layering, the limited documentation of growth zoning in S_{1a} minerals, and the absence of S_2 minerals and foliation, which suggests a lack of subsequent M_2 retrograde re-equilibration of this sample.

Another large (9 kg) sample of Lake Harbour Group metapelite (D024; Fig. 5) containing an S_2 sillimanite–biotitez–plagioclase–quartz–K-feldspar–garnet–cordierite–melt assemblage, and exhibiting a well-developed, penetrative, sub-millimetre-scale foliation, was also analysed by XRF to determine its bulk-rock composition (Thériault *et al.*, 2001). We are aware that the growth of overprinting assemblages and the imposition of chemical zoning in porphyroblasts during subsequent metamorphic

Downloaded from http://petrology.oxfordjournals.org/ by guest on June 7, 2013

Table 5: Plagioclase analyses

	D515C	D515R	S502C	S502R	N503AR	N503BR	D518C	D518R	D527C	D527R	E501C	E501R	J501C	J501R	N516C	N516R	M500C	M500R	P501C	P501R	S501C	S501R
SiO_2	59·50	60·28	58·39	58·59	54·67	54·39	60·31	59·76	59·18	59·23	58·60	59·36	58·88	58·28	58·97	59·42	60·44	60·20	58·32	58·32	58·83	57·92
Al_2O_3	24·36	24·49	25·56	25·65	27·75	27·46	25·07	24·71	24·83	24·88	25·06	25·04	25·12	25·29	24·72	25·11	24·00	23·72	25·50	25·45	25·34	24·97
Na_2O	8·33	8·40	7·21	7·69	6·04	5·97	8·15	8·47	7·66	8·24	7·91	8·04	8·04	8·10	8·06	8·21	8·49	8·66	7·65	7·37	7·67	8·23
CaO	5·57	5·55	7·54	7·17	9·84	9·44	6·62	6·30	6·72	6·61	6·73	6·58	6·76	6·76	6·46	6·38	5·61	5·41	7·17	7·20	6·50	6·69
K_2O	0·16	0·26	0·19	0·20	0·31	0·44	0·25	0·13	0·18	0·11	0·17	0·17	0·11	0·16	0·07	0·10	0·14	0·17	0·24	0·22	0·11	0·14
BaO	0·16	0·11	0·15	0·00	0·00	0·00	0·07	0·02	0·01	0·00	0·21	0·02	0·00	0·05	0·10	0·00	0·04	0·00	0·14	0·02	0·00	0·00
SrO	0·10	0·01	0·23	0·10	0·10	0·26	0·26	0·00	0·06	0·00	0·00	0·11	0·14	0·01	0·06	0·04	0·10	0·15	0·00	0·01	0·04	0·18
FeO	0·00	0·04	0·00	0·00	0·11	0·22	0·00	0·01	0·02	0·11	0·01	0·01	0·05	0·11	0·00	0·01	0·03	0·05	0·02	0·09	0·03	0·04
Total	98·18	99·14	99·27	99·40	98·82	98·18	100·73	99·40	98·66	99·18	98·69	99·33	99·10	98·76	98·44	99·27	98·85	98·36	99·04	98·68	98·52	98·17
Cations normalized for 32 oxygens																						
Si	10·80	10·82	10·54	10·54	9·99	10·01	10·71	10·73	10·70	7·95	10·62	10·67	10·62	10·56	10·69	10·68	10·88	10·90	10·54	10·56	10·64	10·57
Al	5·21	5·18	5·44	5·44	5·98	5·96	5·25	5·23	5·29	7·97	5·35	5·31	5·34	5·40	5·28	5·32	5·09	5·06	5·43	5·43	5·40	5·37
Na	2·93	2·93	2·52	2·68	2·14	2·13	2·81	2·95	2·69	4·35	2·78	2·80	2·81	2·85	2·83	2·86	2·97	3·04	2·68	2·59	2·69	2·91
Ca	1·08	1·07	1·46	1·38	1·93	1·86	1·26	1·21	1·30	1·93	1·31	1·27	1·31	1·31	1·25	1·23	1·08	1·05	1·39	1·40	1·26	1·31
K	0·04	0·06	0·05	0·05	0·07	0·10	0·06	0·03	0·04	0·04	0·04	0·04	0·03	0·04	0·02	0·02	0·03	0·04	0·06	0·05	0·03	0·03
Ba	0·01	0·01	0·01	0·00	0·00	0·00	0·01	0·00	0·00	0·00	0·02	0·00	0·00	0·00	0·01	0·00	0·00	0·00	0·01	0·00	0·00	0·00
Sr	0·01	0·00	0·02	0·01	0·01	0·03	0·03	0·00	0·01	0·00	0·00	0·01	0·02	0·00	0·01	0·01	0·01	0·02	0·00	0·00	0·01	0·02
Fe	0·00	0·01	0·00	0·00	0·02	0·03	0·00	0·00	0·00	0·03	0·00	0·00	0·01	0·02	0·00	0·00	0·00	0·01	0·00	0·01	0·01	0·01
Ab	71·94	71·99	62·13	65·10	51·57	51·64	67·53	70·33	66·55	68·86	67·14	67·99	67·61	67·74	68·81	69·46	72·44	73·35	64·83	64·04	67·59	68·16
An	26·61	26·29	35·90	33·54	46·41	45·16	30·31	28·93	32·23	30·52	31·58	30·74	31·40	31·26	30·46	29·86	26·44	25·32	33·58	34·60	31·66	30·63
Or	0·93	1·48	1·11	1·09	1·76	2·52	1·40	0·72	1·02	0·62	0·92	0·95	0·63	0·88	0·41	0·56	0·81	0·94	1·35	1·29	0·63	0·77
Ba	0·27	0·20	0·27	0·00	0·00	0·00	0·12	0·02	0·02	0·00	0·36	0·02	0·00	0·10	0·17	0·00	0·07	0·00	0·24	0·05	0·00	0·00
Sr	0·25	0·05	0·59	0·27	0·26	0·68	0·65	0·00	0·17	0·00	0·00	0·29	0·36	0·02	0·15	0·12	0·24	0·39	0·00	0·02	0·13	0·44
Event	M_{1a}	M_{1a}	M_{1a}	M_{1a}	M_{1a}	M_{1a}	M_2	M_2	M_2	M_2	M_2	M_2	M_2	M_2	M_2	M_2	M_{1a}	M_2	M_{1a}	M_2	M_{1a}	M_2

Labels refer to samples; C, core; R, rim.

Downloaded from http://petrology.oxfordjournals.org/ by guest on June 7, 2013

Table 6: Biotite analyses

	D515C	D515R	S502C	S502R	N503AR	N503BR	D518C	D518R	D527C	D527R	E501C	E501R	J501C	J501R	N516C	N516R	M500C	M500R	P501C	P501R	S501C	S501R
SiO_2	35·79	35·26	36·63	37·48	34·15	35·20	34·12	35·45	36·96	36·06	36·00	36·02	36·14	34·94	35·83	35·02	38·23	37·29	35·34	35·62	35·54	35·03
Al_2O_3	16·57	16·58	15·37	14·76	14·06	13·94	16·91	17·36	15·24	15·36	15·76	15·91	15·35	15·42	17·21	16·79	16·21	15·84	16·10	17·41	16·18	16·25
Cr_2O_3	0·10	0·07	0·18	0·17	0·03	0·04	0·13	0·14	0·08	0·07	0·03	0·07	0·12	0·15	0·17	0·16	0·78	0·69	0·39	0·38	0·10	0·10
TiO_2	4·63	4·63	4·66	4·93	4·90	4·80	4·18	4·28	4·31	4·85	3·66	3·72	4·25	5·29	3·28	4·18	3·86	3·84	5·18	4·31	4·21	4·16
Fe_2O_3	7·09	9·12	3·07	0·00	10·47	5·81	11·30	6·45	7·17	9·86	7·80	7·46	6·18	9·17	10·56	10·63	6·89	7·58	5·91	6·99	6·87	9·52
FeO	8·56	7·19	8·64	11·37	12·39	16·26	6·65	11·43	5·38	2·70	5·41	5·73	6·86	5·44	5·80	7·13	2·00	0·96	9·37	8·68	8·05	6·09
MnO	0·06	0·04	0·04	0·00	0·00	0·08	0·04	0·03	0·00	0·00	0·00	0·05	0·02	0·00	0·05	0·08	0·04	0·03	0·09	0·02	0·00	0·00
MgO	12·15	11·98	14·40	12·92	9·23	9·11	10·74	10·05	15·66	15·67	14·64	14·44	14·34	13·21	12·72	11·41	17·89	17·84	11·62	11·50	12·63	12·66
CaO	0·00	0·00	0·00	0·12	0·00	0·06	0·02	0·01	0·01	0·07	0·01	0·03	0·02	0·06	0·00	0·01	0·00	0·03	0·00	0·06	0·01	0·00
Na_2O	0·10	0·11	0·18	0·15	0·01	0·07	0·08	0·09	0·11	0·11	0·08	0·15	0·12	0·05	0·14	0·15	0·07	0·06	0·08	0·07	0·11	0·11
K_2O	6·97	6·81	6·75	6·30	6·77	6·70	6·75	6·86	6·88	6·97	6·98	6·97	6·68	6·79	6·70	6·87	7·03	7·05	6·77	6·95	6·87	6·93
Total	92·02	91·79	89·92	88·20	92·01	92·07	90·92	92·15	91·80	91·72	90·37	90·55	90·08	90·52	92·46	92·43	93·00	91·21	90·85	91·99	90·57	90·85
Cations normalized to 22 oxygens																						
Si	5·40	5·33	5·58	5·82	5·33	5·51	5·24	5·40	5·50	5·36	5·46	5·46	5·50	5·33	5·35	5·29	5·51	5·48	5·41	5·38	5·43	5·34
Al	3·55	3·62	3·18	2·88	2·59	3·06	3·82	3·72	3·17	3·33	3·36	3·38	3·25	3·45	3·68	3·70	3·24	3·27	3·50	3·72	3·48	3·58
Cr	0·01	0·01	0·02	0·02	0·00	0·01	0·02	0·02	0·01	0·01	0·00	0·01	0·01	0·02	0·02	0·02	0·09	0·08	0·05	0·05	0·01	0·01
Ti	0·53	0·53	0·53	0·58	0·58	0·57	0·48	0·49	0·48	0·54	0·42	0·42	0·49	0·61	0·37	0·47	0·42	0·42	0·60	0·49	0·48	0·48
Fe^{3+}	0·81	1·04	0·35	0·00	1·23	0·68	1·31	0·74	0·80	1·10	0·89	0·85	0·71	1·05	1·19	1·21	0·75	0·84	0·68	0·79	0·79	1·09
Fe^{2+}	1·08	0·91	1·10	1·48	1·62	2·13	0·85	1·46	0·67	0·34	0·69	0·73	0·87	0·69	0·72	0·90	0·24	0·12	1·20	1·10	1·03	0·78
Mn	0·01	0·01	0·01	0·00	0·00	0·01	0·01	0·00	0·00	0·00	0·00	0·01	0·00	0·00	0·01	0·01	0·01	0·00	0·01	0·00	0·00	0·00
Mg	2·73	2·70	3·27	2·99	2·15	2·13	2·46	2·28	3·47	3·47	3·31	3·26	3·26	3·00	2·83	2·57	3·85	3·91	2·65	2·59	2·88	2·88
Ca	0·00	0·00	0·00	0·02	0·00	0·01	0·00	0·00	0·00	0·01	0·00	0·01	0·00	0·01	0·00	0·00	0·00	0·01	0·00	0·01	0·00	0·00
Na	0·03	0·03	0·06	0·05	0·00	0·02	0·02	0·03	0·03	0·03	0·02	0·04	0·04	0·02	0·04	0·04	0·02	0·02	0·02	0·02	0·03	0·03
K	1·34	1·31	1·31	1·25	1·35	1·34	1·32	1·33	1·31	1·32	1·35	1·35	1·30	1·32	1·28	1·32	1·29	1·32	1·32	1·34	1·34	1·35
mg-no.	0·59	0·58	0·69	0·67	0·43	0·43	0·53	0·51	0·70	0·71	0·68	0·67	0·67	0·63	0·60	0·55	0·80	0·80	0·59	0·58	0·61	0·61
Event	M_{1a}	M_{1a}	M_{1a}	M_{1a}	M_{1a}	M_{1a}	M_2	M_2	M_2	M_2	M_2	M_2	M_2	M_2	M_2	M_2	M_{1a}	M_2	M_{1a}	M_2	M_{1a}	M_2

Labels refer to samples; C, core; R, rim. *mg*-no. $= Mg/(Mg + Fe^{2+} + Fe^{3+})$. Fe^{3+} is derived from charge-balance calculation.

Downloaded from http://petrology.oxfordjournals.org/ by guest on June 7, 2013

events (i.e. M_2), may render such data inappropriate for the calculation of phase diagrams because of the possibility that porphyroblast cores may no longer be in equilibrium with surrounding matrix minerals. However, the strong development of a penetrative S_2 schistose foliation in sample D024, which by analogy with other samples in this study (e.g. D518, D527, E501, J501, and N516) points to an exclusively M_2 origin, suggests that the whole-rock XRF data can be considered to approximate the effective bulk composition during the overprinting metamorphic event (e.g. Stüwe, 1997; Marmo *et al.*, 2002). In other words, based on the textural criteria available, D024 is interpreted to have completely re-equilibrated during the younger M_2 metamorphic event.

U–Pb geochronology

Eight samples of metasedimentary and metaplutonic rocks from the Lake Harbour Group and four samples of felsic intrusive rocks were studied for U–Pb geochronology using isotope dilution thermal ionization mass spectrometry (ID-TIMS) at the GSC. Sample locations are given in Fig. 5. Preliminary results for three of the eight metasedimentary and metaplutonic samples (N056, D094B, N312) were presented by Wodicka & Scott (1997), Scott & Wodicka (1998) and Davis *et al.* (1998). Zircon, monazite, and titanite were separated by standard crushing, grinding, hydrodynamic, and heavy liquid techniques. Purification of the heavy mineral concentrates was carried out using a Frantz LB-1 isodynamic separator. All zircon fractions and some monazite and titanite fractions were air abraded following the method of Krogh (1982). The analytical methods for U–Pb analysis of zircon and monazite have been summarized by Parrish *et al.* (1987) and those of titanite in Davis *et al.* (1997). Treatment of analytical errors follows that outlined by Roddick (1987), with regression analysis modified after York (1969). For samples whose analyses are concordant or nearly concordant within error, the cited age is the weighted average of the $^{207}Pb/^{206}Pb$ ages (or $^{207}Pb/^{235}U$ ages in the case of reversely discordant monazite analyses), calculated using Isoplot version 3.00 of Ludwig (2003). Decay constants used are those recommended by Steiger & Jäger (1977).

Back-scattered electron (BSE) images were obtained from selected grains of monazite to evaluate the dispersion of ages obtained from two samples (N056 and D332A). Imaging was carried out on a Cambridge Instruments S360 scanning electron microprobe also located at the GSC. Operating conditions were 20 kV accelerating voltage and 2–5 nA beam current. Most images reveal internal compositional variations that reflect differences in the average atomic number of monazite. Based on several monazite studies (e.g. Zhu *et al.*, 1997; Stern & Sanborn, 1998; Foster *et al.*, 2002), these differences largely reflect differences in the concentration of rare earth elements (REE), U, and especially Th.

RESULTS

Thermobarometry

S_{1a} assemblages

Four of the analysed samples contain exclusively S_{1a} mineral assemblages, with two samples characterized by a well-developed compositional foliation (D515, S502), two by a weakly developed planar foliation (N503A, N503B), and all four devoid of overprinting S_2 assemblages and modification by S_2 fabrics (Table 1). The two well-layered samples are pelitic (D515, S502) whereas the two foliated samples are mafic (N503A, N503B). All four yield relatively high T and P estimates (Table 7) with average determinations of 812°C and 7·5 kbar for mineral core compositions and 810°C and 8·3 kbar for mineral rim compositions. If one includes the P–T estimates based on S_{1a} mineral core compositions from three samples (M500, P501, S501; Table 7) that contain overprinting S_2 (rim) assemblages, the average mineral core P–T determinations for S_{1a} remain virtually unchanged at 806°C and 7·6 kbar.

S_2 assemblages

Five analysed samples contain exclusively S_2 mineral assemblages that define (biotite, sillimanite, plagioclase) and overgrow (garnet) a well-developed schistose foliation (Fig. 6b; Table 1). The five samples (D518, D527, E501, J501, N516) yield lower T and P estimates (Table 7) when compared with the P–T determinations for S_{1a} (cores and rims) presented above, with average S_2 determinations of 735°C and 6·5 kbar for mineral core compositions and 710°C and 6·0 kbar for mineral rim compositions. In contrast to the thermobarometric results for S_{1a}, the S_2 data document a slight decrease in both P and T from mineral core to mineral rim analyses.

Phase diagrams

To further delimit potential segments of P–T paths as derived from core–rim thermobarometry and to substantiate the apparently contrasting trends in recorded P–T evolution for the M_{1a} and M_2 events (see above), two phase diagrams were constructed for the pelitic rocks of the study area (Figs 8–11) utilizing the XRF data presented by Thériault *et al.* (2001). As the samples in that study were completely consumed by the whole-rock chemical analysis, subsequent direct thermobarometric work was not an option and consequently some degree of mismatch might be expected when comparing predicted compositional mineral trends with those observed in the analysed thermobarometric samples.

S_{1a} assemblages

The phase diagram based on the bulk-rock composition of sample N016 (Fig. 5) and for which saturation of the H_2O content in the system occurs just below solidus, is shown

Downloaded from http://petrology.oxfordjournals.org/ by guest on June 7, 2013

Table 7: P–T estimates

Sample no.*	Foliation	Event	*P* (kbar)†	SD (kbar)‡	*T* (°C)†	SD (°C)†	Equilibria
S_{1a} granulite-facies assemblage							
D515C	well-developed S_{1a}	M_{1a}	7·5	0·4	810	31	1, 2, 3, 4
D515R	well-developed S_{1a}	M_{1a}	8·3	0·3	801	23	1, 2, 3, 4
S502C	well-developed S_{1a}	M_{1a}	7·5		814		1, 3
S502R	well-developed S_{1a}	M_{1a}	8·1		847		1, 3
N503AR	weakly developed S_{1a}	M_{1a}	8·3	0·8	790	38	1, 5, 6, 7, 8, 9
N503BR	weakly developed S_{1a}	M_{1a}	8·4	0·9	797	4	1, 5, 6, 7, 8, 9
S_2 amphibolite-facies assemblage							
D518C	pervasive S_2	M_2	7·0	1·0	753	17	1, 2, 3, 4
D518R	pervasive S_2	M_2	5·0	0·5	666	24	1, 2, 3, 4
D527C	pervasive S_2	M_2	6·3		733		1, 3
D527R	pervasive S_2	M_2	6·1		717		1, 3
E501C	pervasive S_2	M_2	6·2		718		1, 3
E501R	pervasive S_2	M_2	6·5		734		1, 3
J501C	pervasive S_2	M_2	6·4	0·3	717	22	1, 2, 3, 4
J501R	pervasive S_2	M_2	6·3	0·5	714	6	1, 2, 3, 4
N516C	pervasive S_2	M_2	6·4	0·4	764	26	1, 2, 3, 4
N516R	pervasive S_2	M_2	5·9	0·0	718	2	1, 2, 3, 4
S_{1a} granulite-facies assemblage overprinted by S_2 amphibolite-facies assemblage							
M500C	well-developed S_{1a}	M_{1a}	8·4	0·2	790	11	1, 2, 3, 4
M500R	moderate S_2 overprint	M_2	7·7	0·1	717	7	1, 2, 3, 4
P501C	well-developed S_{1a}	M_{1a}	7·6	0·3	829	19	1, 2, 3, 4
P501R	moderate S_2 overprint	M_2	6·9	0·7	758	4	1, 2, 3, 4
S501C	well-developed S_{1a}	M_{1a}	6·9	0·4	789	27	1, 2, 3, 4
S501R	moderate S_2 overprint	M_2	6·3	0·3	734	16	1, 2, 3, 4

*C, mineral core analyses; R, mineral rim analyses.
†Calculated using the TWEEQU database (Berman, 1991).
‡The 1·0σ standard deviation calculated by the INTERSX program (Berman, 1991).

in Fig. 8. The bulk-rock composition for N016, which contained only an S_{1a} granulite-facies mineral assemblage and an associated, well-developed compositional foliation, restricts the garnet–cordierite–biotite–sillimanite–plagioclase–K-feldspar–quartz–melt assemblage to a specific stability field, which is highlighted with a dashed line. The average S_{1a} (core) P–T determination derived from the thermobarometric results presented above is plotted as point 'C' in Fig. 8 and is in good agreement with the outlined stability field for this assemblage. In contrast, the average S_{1a} (rim) P–T determination (point 'R' in Fig. 8) lies above the outlined stability field within the higher-P garnet–biotite–sillimanite–plagioclase–quartz–melt (cordierite absent) field. As previously noted, all phases defining the S_{1a} assemblage appear to be in mutual textural equilibrium, with the exception of cordierite (Fig. 7b). Thus the increase in P during M_{1a} as recorded by the thermobarometric results in Table 7, and the inferred consequent instability of cordierite as shown in the phase diagram of Fig. 8, appear to be corroborated texturally by the recessive and embayed aspect of S_{1a} cordierite in thin section as previously described. The increase in P during M_{1a} is also consistent with the minor increase in the grossular content of garnet from core to rim in analysed S_{1a} samples D515 and S502 (Table 3).

The essentially isothermal compressive P–T path segment for M_{1a} as defined by core to rim thermobarometry (Fig. 8) can be corroborated by the isopleths of $Mg/(Mg+Fe)$ and X_{Grs} calculated for sample N016 and shown for the relevant garnet-bearing portion of the phase diagram in Fig. 9. The core to rim segment of the path (continuous-line arrow) can be seen to follow at a small angle the $Mg/(Mg+Fe)$ isopleths for garnet (Fig. 9a), which agrees with the small to negligible increase in the Mg number from analysed S_{1a} garnet cores to rims (Table 3). Likewise, the core to rim P–T path segment crosses a field characterized by a slight increase

Downloaded from http://petrology.oxfordjournals.org/ by guest on June 7, 2013

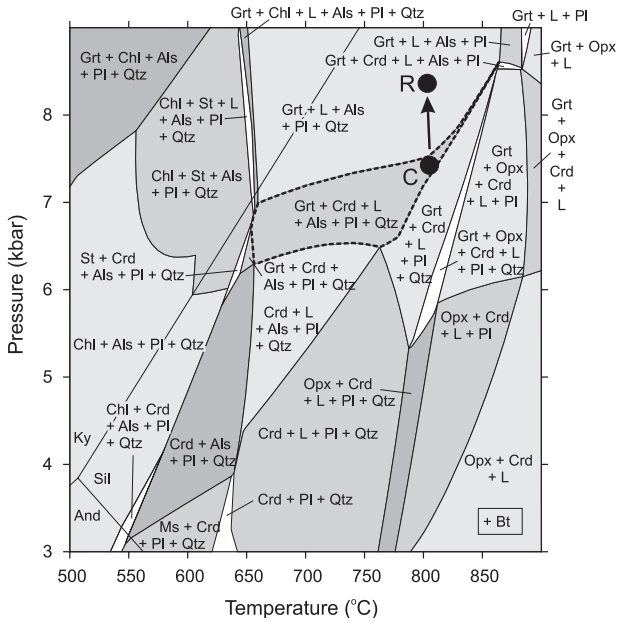


Fig. 8. Phase diagram calculated with the DOMINO software (De Capitani, 1994) for S_{1a} sample N016 (bulk composition in mole%: SiO_2 61·15, Al_2O_3 24·46, FeO 7·98, MgO 14·10, CaO 0·23, K_2O 7·08, Na_2O 1·54, MnO 0·00). All stability fields include biotite. The H_2O content in the system was reduced to the point that the assemblage was just saturated immediately subsolidus, following the procedure reported by White *et al.* (2001). Some stability fields less than a few degrees in width have been omitted for clarity. Shading of stability fields is independent of variance. Continuous-line segment of P–T path is based on mineral core (C) and rim (R) thermobarometric determinations for M_{1a} samples (D515, N503A/B, and S502) as discussed in the text. Outlined stability field is that for the assemblage garnet–cordierite–biotite–sillimanite–plagioclase–K-feldspar–quartz–melt. Mineral abbreviations in this and following figures are after Kretz (1983).

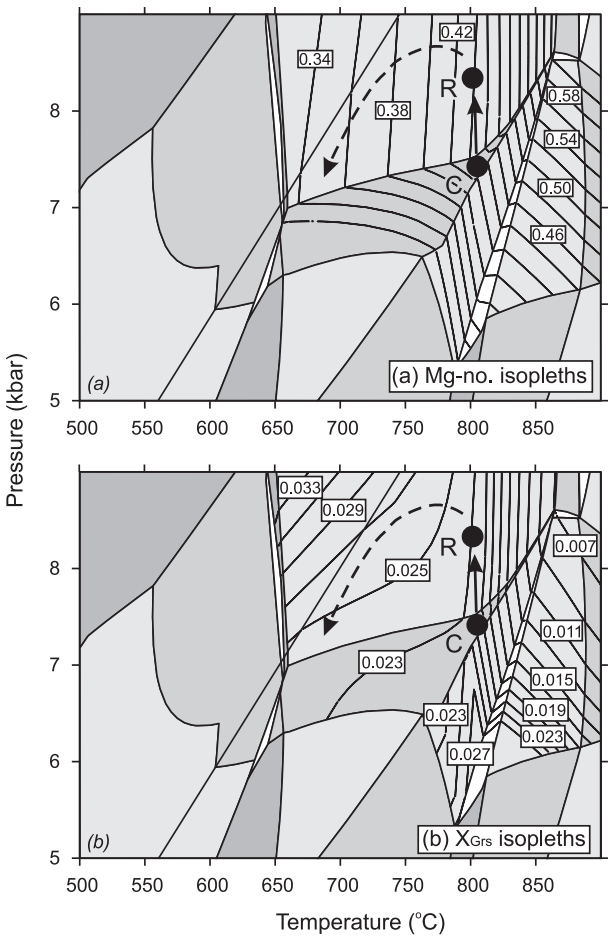


Fig. 9. Detail of phase diagram calculated for sample N016 showing (a) isopleths of Mg/(Mg + Fe) and (b) X_{Grs} for the garnet stability field of Fig. 8. Mineral assemblage stability fields are the same as those shown in Fig. 8 (upper half). The dashed-line segment of the P–T path is based on petrographic interpretation and the general trend in analysed garnet compositions as discussed in text.

in X_{Grs}, as documented by the isopleths of Fig. 9b and reflected in the S_{1a} garnet analyses of Table 3. Finally, the absence of kyanite in S_{1a} assemblages within the project area suggests that the subsequent cooling path remained within the sillimanite stability field and approximated the P–T path segment shown with a dashed line in Fig. 9.

S_2 assemblages

The phase diagram based on the bulk-rock composition of sample D024 (Fig. 5), and for which saturation of the H_2O content in the system occurs just below solidus, is shown in Fig. 10. The bulk-rock composition for D024, which containes an S_2 biotite–sillimanite–cordierite–garnet–quartz–melt mineral assemblage and a pervasive, well-developed schistose foliation, limits the S_2 assemblage to the stability field that is highlighted with a dashed line in Fig. 10. The thermobarometric conditions determined with S_2 core and rim mineral analyses (points 'C' and 'R' in Fig. 10) plot just outside the stability field determined from the bulk-rock composition, suggesting either that sillimanite may have equilibrated early along the P–T path for M_2 (shown in Fig. 10 with a dashed P–T path line segment) or that the bulk-rock composition for sample D024 does not adequately approximate the effective bulk composition (e.g. Stüwe, 1997; Marmo *et al.*, 2002) for the Lake Harbour Group pelites during M_2. The abundant fine-grained sillimanite defines the S_2 foliation in all thin sections examined and thus appears to be in textural equilibrium with adjacent S_2 biotite, cordierite, and plagioclase grains (Fig. 6b). In contrast, sillimanite is never observed in direct contact with the S_2 garnet, the two mineral phases generally being separated by intervening plagioclase, cordierite, or biotite grains. The latter observation suggests that sillimanite may have indeed equilibrated early along the M_2 path and become a relict phase prior to growth of the small, sub-equant S_2 garnets.

Downloaded from http://petrology.oxfordjournals.org/ by guest on June 7, 2013

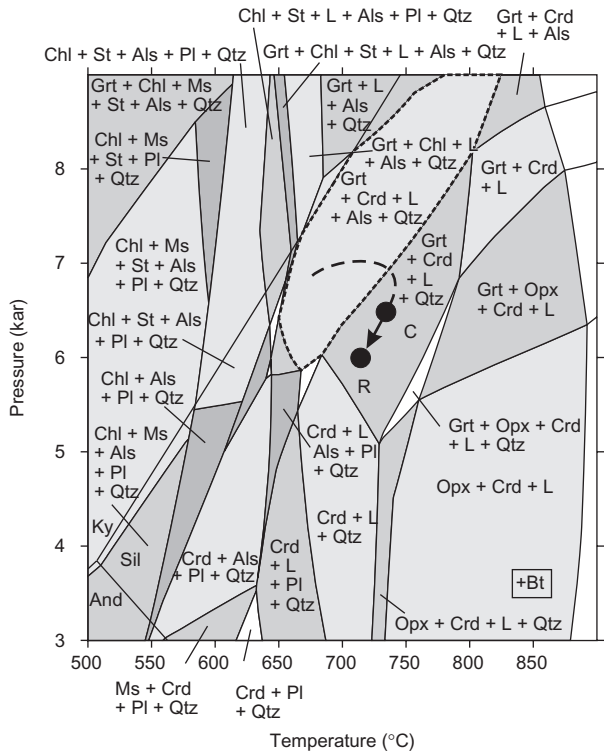


Fig. 10. Phase diagram calculated with the DOMINO software (De Capitani, 1994) for S_2 sample D024 (bulk composition in mole%: SiO_2 62·53, Al_2O_3 29·10, FeO 7·32, MgO 12·19, CaO 0·04, K_2O 4·56, Na_2O 2·20, MnO 0·00). All stability fields in the shaded portion of the diagram include biotite. The H_2O content in the system was reduced to the point that the assemblage was just saturated immediately subsolidus, following the procedure reported by White *et al.* (2001). Some stability fields less than a few degrees in width have been omitted for clarity. Shading of stability fields is independent of variance. Continuous-line segment of P–T path is based on mineral core (C) and rim (R) thermobarometric determinations for M_2 samples (D518, D527, E501, J501, N516) as discussed in the text. Outlined stability field is that for the assemblage garnet–cordierite–biotite–sillimanite–plagioclase–K-feldspar–quartz–melt.

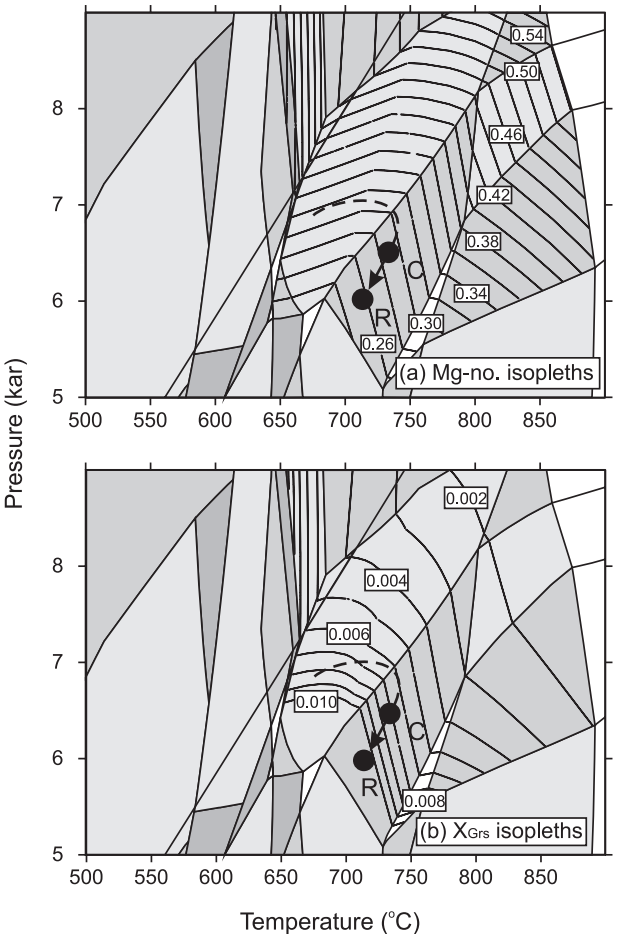


Fig. 11. Detail of phase diagram calculated for sample D024 showing isopleths of (a) Mg/(Mg + Fe) and (b) X_{Grs} for the garnet stability field of Fig. 10. Mineral assemblage stability fields are the same as those shown in Fig. 10 (upper half). Dashed-line segment of P–T path based on petrographic interpretations as discussed in the text.

The M_2 P–T path segment derived by thermobarometry is corroborated by the isopleths of Mg/(Mg + Fe), but less so by X_{Grs}, as calculated for sample D024 and shown for the relevant garnet-bearing portion of the phase diagram in Fig. 11. The core to rim segment of the path (continuous-line arrow) can be seen to cross at a high angle the Mg/(Mg + Fe) isopleths for garnet (Fig. 11a), which agrees with the decrease in the Mg number for most analysed S_2 garnet cores to rims (Table 3). The P–T path segment also crosses at high angles the X_{Grs} isopleths for D024 (Fig. 11b), suggestive of an increase in Ca content from core to rim. Such a compositional trend is documented in only one S_2 sample (N516, Table 3) with most other S_2 garnet grains actually showing a decrease in Ca from core to rim. This apparent contradiction in predicted vs actual grossular compositional trends for S_2 garnets is interpreted to reflect the variable nature of the metasomatic processes associated with the retrograde M_2 metamorphic event, making our assumption of a representative M_2 effective bulk composition largely invalid, at least in terms of Ca content. Alternatively, the bulk-rock composition derived from sample D024 may simply not be representative of the analysed S_2 pelite samples in the study area.

U–Pb geochronology

Twelve samples of Lake Harbour Group metasedimentary rocks and associated felsic intrusive units from the study area were analysed for U–Pb geochronology. Details pertaining to the morphology, colour, and chemistry of the analysed mineral phases are given in Electronic Appendix 1 (http://www.petrology.oxfordjournals.org). The results presented below, and summarized in Table 8, document the timing and duration of the M_{1a} and M_2 metamorphic events, the associated formation of the S_{1a}

Downloaded from http://petrology.oxfordjournals.org/ by guest on June 7, 2013

Table 8: Available U–Pb geochronological data from the study area (Meta Incognita microcontinent), southern Baffin Island

Unit, rock type	Mineral	Age (Ma)	(Re-)interpretation	Reference
Ramsay River orthogneiss				
Monzogranite gneiss	Zrn	1950 +6/–4	crystallization age	Scott & Wodicka (1998)
	Zrn	1832 ± 12	M_{1b} metamorphism (?)	Scott & Wodicka (1998)
Lake Harbour Group				
Psammite	Zrn	1937 ± 4	max. age of deposition	Scott & Wodicka (1998)
Psammite	Zrn	1934 ± 2	max. age of deposition	Scott & Gauthier (1996)
	Zrn	1833 ± 2	M_{1b} metamorphism (?)	Scott & Gauthier (1996)
	Zrn	1785 ± 18	M_2 (?) metamorphic overgrowth	Scott *et al*. (2002)
Grt–Crd–Bt–Sil pelite (S502)	Mnz	1849–1844	M_{1a} metamorphism	This study
	Mnz	1830 ± 2	M_{1b} metamorphism (?)	This study
Monzogranite melt pod	Mnz	1845 ± 2	M_{1a} metamorphism (partial melting)	Scott (1997)
White monzogranite vein	Mnz	1845 ± 2	M_{1a} metamorphism (partial melting)	Wodicka & Scott (1997)
Semipelite (D332A)	Mnz	>1845 ± 2	M_{1a} metamorphism	This study
	Mnz	1813 ± 2	M_2 metamorphism	This study
Psammite	Mnz	1844 ± 2	M_{1a} metamorphism	Wodicka & Scott (1997)
	Zrn	1819 ± 15	M_2 metamorphism	Scott *et al*. (2002)
White monzogranite (N056)	Mnz/Zrn	>1841 ± 2	M_{1a} metamorphism (partial melting)	This study
	Mnz/Zrn	1820 ± 1	M_2 metamorphism	This study
Grey psammite (D513B)	Mnz	>1839–1835	M_{1a} metamorphism	This study
Grey psammite (N311)	Mnz	>1838 ± 2	M_{1a} metamorphism	This study
White monzogranite (D094B)	Mnz/Zrn	1837 + 2/–1	M_{1a} metamorphism (partial melting)	This study
	Zrn	>1818 ± 2	M_2 metamorphism	This study
Orthoquartzite	Mnz	1814 ± 2	M_2 metamorphism	Wodicka & Scott (1997)
Psammite	Zrn	1779 ± 47	M_2 (?) metamorphic overgrowth	Scott *et al*. (2002)
Siliceous marble (D020)	Ttn	1790 ± 1	post-D_2 thermal/fluid activity	This study
Metagabbro (D513A)	Ttn	1785 ± 4	post-D_2 thermal/fluid activity	This study
Blandford Bay assemblage				
Semipelite	Mnz	1844 ± 1	M_{1a} metamorphism	Wodicka & Scott (1997)
Orthoquartzite	Mnz	1829 ± 2	M_{1b} metamorphism (?)	Wodicka & Scott (1997)
Tonalite vein	Zrn	1819 ± 4	M_2 metamorphism (partial melting)	Wodicka & Scott (1997)
Cumberland batholith				
Opx monzogranite	Zrn	1865 +4/–2	crystallization age	Scott & Wodicka (1998)
Pink monzogranite	Zrn	1850 +5/–4	crystallization age	Wodicka & Scott (1997)
	Mnz	1832 ± 2	cooling	Wodicka & Scott (1997)
Monzogranite vein	Zrn	1848 ± 2	crystallization age	Scott & Wodicka (1998)
	Mnz	1843 ± 1	cooling	Wodicka & Scott (1997)
Felsic intrusive rocks				
Syenogranite pegmatite (D534)	Zrn/Mnz	1844 +9/–3	crystallization age (late S_{1a})	This study
Monzogranite dyke	Mnz	1840 ± 3	crystallization age (late to post-S_{1a})	Scott (1997)
Opx monzonite (N312)	Zrn	1834 ± 1	crystallization age (post-S_{1a})	This study
	Zrn	*ca*. 1830	post-intrusion M_{1b} metamorphism	This study
	Zrn/Mnz	1816 +2/–1	M_2 metamorphism	This study
	Zrn	1797 ± 2	post-D_2 thermal/fluid activity	This study
	Mnz	1791 ± 2	post-D_2 thermal/fluid activity	This study
Monzogranite pegmatite (D532)	Zrn/Mnz	1833 ± 1	crystallization age (post-S_{1a})	This study
Syenite plug (D533)	Zrn	1831 ± 3	crystallization age (post-S_{1a})	This study
Sheet-like syenite intrusion	Zrn	1784 +7/–9	crystallization age (late-S_2)	Scott (1997)
Syenogranite pegmatite	Mnz	>1760 ± 2	min. crystallization age (post-D_2)	Scott (1997)

Mineral abbreviations are after Kretz (1983).

Downloaded from http://petrology.oxfordjournals.org/ by guest on June 7, 2013

and S_2 deformation fabrics, and further characterize the polymetamorphic evolution of the study area.

White monzogranites, Lake Harbour Group

Siliciclastic rocks of the Lake Harbour Group are typically associated with white monzogranite occurring either as discrete, metre-thick tabular bodies or as concordant to sub-concordant layers or irregular pods less than 0·5 m thick and generally aligned parallel to, and wrapped by, the dominant S_{1a} compositional foliation in the metasedimentary host. The monzogranite contains garnet with or without minor biotite, cordierite, and sillimanite. The aluminous mineral assemblage, the field association with the Lake Harbour Group, and the relationship to the dominant S_{1a} compositional foliation suggest a derivation by partial melting during M_{1a} regional metamorphism (e.g. St-Onge *et al.*, 1996; Scott, 1997). Both zircon and monazite were recovered from two samples of white monzogranite (N056, D094B; Fig. 5) making these rocks suitable for documenting the timing of M_{1a} metamorphism and anatexis.

Sample N056 is from a sheet of garnet-bearing anatectic monzogranite that is concordant to a well-developed S_{1a} compositional foliation in semipelite. The monzogranite lies 500 m north of the trace of a D_2 thrust (Fig. 5) and contains a strong internal S_2 foliation defined by quartz ribbons and millimetre-scale polycrystalline feldspar bands that wrap around large feldspar and S_{1a} garnet porphyroclasts. U–Pb analyses of five unabraded, single-grain fractions of monazite (MA–ME, Fig. 12a) are concordant to near-concordant (0·0–0·3%), but their $^{207}Pb/^{206}Pb$ ages exhibit a range of over 20 Myr between 1841 ± 2 and 1820 ± 2 Ma (Electronic Appendix 1). BSE imaging reveals complex internal structures for euhedral to round monazite grains, with cores showing faint sector, oscillatory, or patchy zoning overgrown by darker homogeneous or faintly zoned rims (Fig. 12b–d). In some cases, irregular embayment boundaries truncate zoning patterns in the core domains without change in the overall shape of the crystal (Fig. 12c and d). In contrast, anhedral fragments tend to be homogeneous (Fig. 12e). These textures, combined with a distinct Th/U ratio–age correlation (Electronic Appendix 1), suggest that the spread in $^{207}Pb/^{206}Pb$ ages exhibited by monazite in sample N056 results largely from recrystallization of older grains combined with younger metamorphic (over)-growth, although the possibility that other processes (e.g. high-temperature Pb loss) were also involved cannot entirely be ruled out. Based on these observations and the petrofabric context for sample N056, the 1841 ± 2 Ma age for the oldest monazite fraction (MB, Fig. 12a) is interpreted as recording the minimum crystallization age of the monzogranite during M_{1a} anatexis (Table 8), with new monazite growth and total recrystallization of M_{1a} grains having occurred at 1820 ± 1 Ma (weighted average $^{207}Pb/^{206}Pb$ age of analyses MC and MD, Table 7; Fig. 12a), possibly in response to fluid influx during the younger M_2 metamorphic event (Table 8).

Two zircon fractions in N056 (ZB and ZC, Fig. 12a) yield the oldest $^{207}Pb/^{206}Pb$ ages of 1836 ± 2 and 1830 ± 2 Ma, respectively, and have low Th/U ratios (Electronic Appendix 1), typical of zircon that has crystallized from hydrous crustal fluids generated during high-grade metamorphism (e.g. Krogh & Davis, 1973). In contrast, two other fractions (ZA and ZD, Fig. 12a) yield distinctly higher Th/U ratios (Table 7) and younger $^{207}Pb/^{206}Pb$ ages of 1808 ± 2 and 1801 ± 6 Ma. The observed differences in chemistry and $^{207}Pb/^{206}Pb$ ages suggest at least two episodes of zircon growth. The age of M_{1a} cannot be determined from the zircon data alone, but the monzogranite is likely to be older than the oldest discordant analysis (ZB) with a $^{207}Pb/^{206}Pb$ age of 1836 ± 2 Ma, consistent with the monazite data from this sample. Regressing the two youngest data points ZA and ZD together with concordant monazite data point MC yields an upper intercept age of 1821 +11/−5 Ma [mean square of weighted deviates (MSWD) = 0·12], indistinguishable from the monazite weighted mean age of 1820 ± 1 Ma for the M_2 event.

Sample D094B (Fig. 5) is a foliated ($S_{1a} + S_2$) anatectic monzogranite sheet containing both monazite and zircon. Wodicka & Scott (1997) originally analysed three single-grain monazite fractions (MA to MC, Fig. 12f) that gave a weighted mean $^{207}Pb/^{206}Pb$ age of 1838 ± 2 Ma. Four additional monazite analyses (MD to MG, Fig. 12f), conducted during subsequent U–Th–Pb studies (Davis *et al.*, 1998; Stern & Sanborn, 1998), showed evidence for isotopic heterogeneity, with fraction MG having a significantly older U/Pb and Pb/Pb age (Electronic Appendix 1). Stern & Sanborn (1998) reported an age estimate of 1836 ± 1 Ma for this sample, based on the non-weighted mean age (1 standard error) of analyses MA to MF. Three multi-grain zircon fractions (ZA–ZC, Fig. 12f) from this same rock show a greater spread in $^{207}Pb/^{206}Pb$ ages and more extensive discordance (0·3–0·7%) than monazite (Electronic Appendix 1), similar to that observed in sample N056. A regression of the most precise collinear zircon and monazite data (fractions ZA, MA, MB, MC, ME, and MF, Fig. 12f) gives an upper intercept of 1837 +2/−1 Ma (MSWD = 1·35). The age determination overlaps both the 1838 ± 2 Ma U–Pb age reported by Wodicka & Scott (1997) and the 1836 ± 1 Ma U–Th–Pb age estimate of Stern & Sanborn (1998). Consequently, 1837 +2/−1 Ma is taken as the best estimate for the crystallization age of the white monzogranite and M_{1a} partial melting at this locality (Table 8). The age for the younger zircon component (ZB and ZC, Fig. 12f) is interpreted to be equal to, or older than the $^{207}Pb/^{206}Pb$ age of the least discordant fraction ZB, which

Downloaded from http://petrology.oxfordjournals.org/ by guest on June 7, 2013

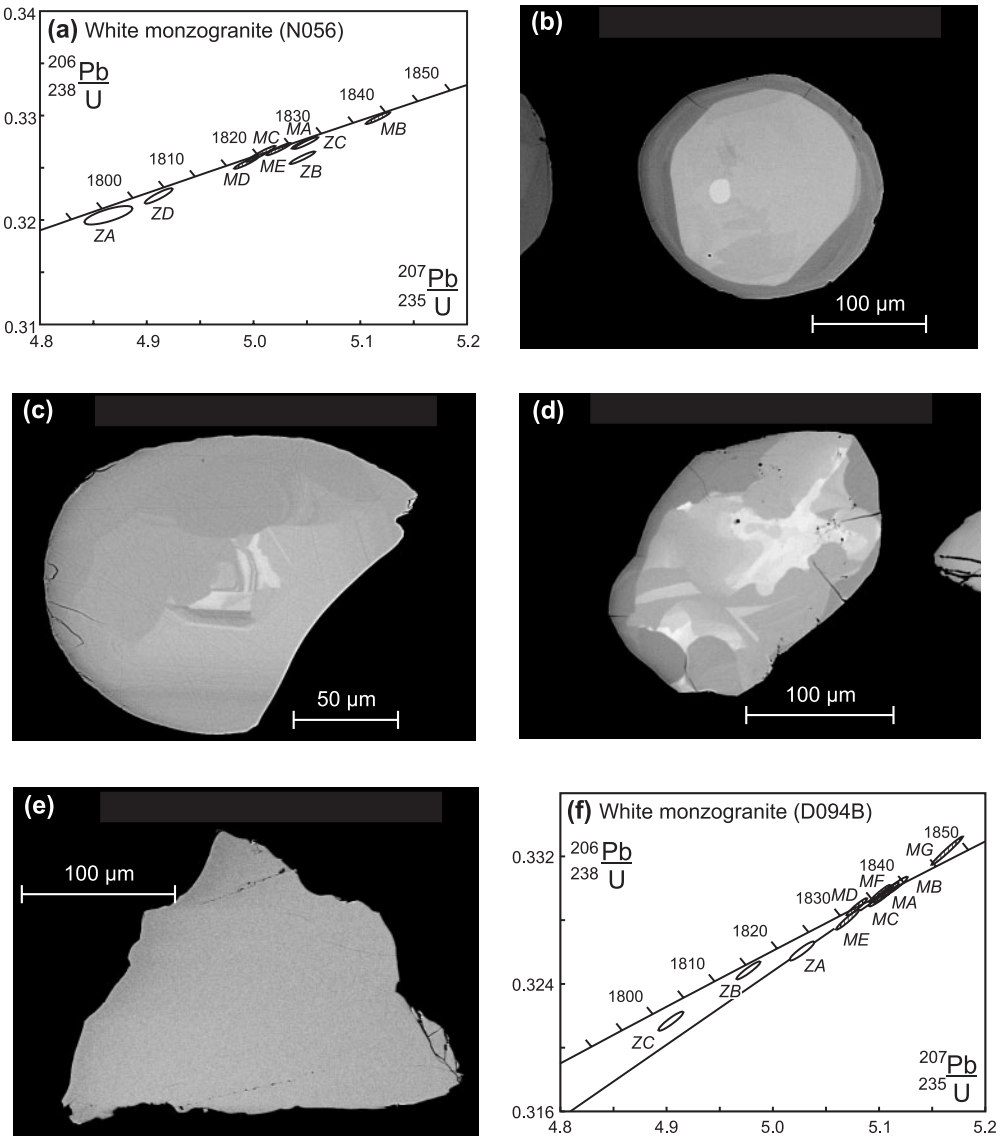


Fig. 12. (a) U–Pb concordia diagram for zircon (white ellipses) and monazite (vertically ruled ellipses) from white monzogranite sample N056. Error ellipses represent 2σ. (b–e) Back-scattered electron (BSE) images of selected monazite crystals from sample N056. (b) Euhedral equant monazite crystal with faint sector zoning overgrown by a concentrically zoned, dark round rim. The bright spot in the centre left of the grain is monazite. (c) Round monazite crystal with embayed oscillatory-zoned central domain. (d) Subhedral monazite crystal showing an irregular, patchy central domain resorbed by inward-directed fronts. (e) Simple homogeneous anhedral monazite fragment with sharp edges. (f) U–Pb concordia diagram for zircon (white ellipses) and monazite (vertically ruled ellipses) from white monzogranite sample D094B. Error ellipses represent 2σ.

is 1818 ± 2 Ma (Table 8). This result corresponds closely to the age determined for M_2 monazite and zircon in sample N056 described above.

Pelitic, semipelitic, and psammitic rocks, Lake Harbour Group

Sample S502 (Fig. 5) is a garnet–biotite–sillimanite–plagioclase–K-feldspar–quartz–melt-bearing metapelite characterized by a well-developed S_{1a} compositional foliation that has yielded core and rim *P–T* estimates of 7·5 kbar and 814°C, and 8·1 kbar and 847°C, respectively (see above; Table 7). Five single-grain monazite analyses (MA–ME, Fig. 13a) define two distinct populations based on their morphology, $^{207}Pb/^{206}Pb$ ages and Th/U ratios (Electronic Appendix 1). The oldest population (MA, MB, MC, ME, Fig. 13a) has slightly discordant (0·1–0·4%) $^{207}Pb/^{206}Pb$ ages in the range 1849 ± 2 to 1844 ± 2 Ma. The second population is defined by a

Downloaded from http://petrology.oxfordjournals.org/ by guest on June 7, 2013

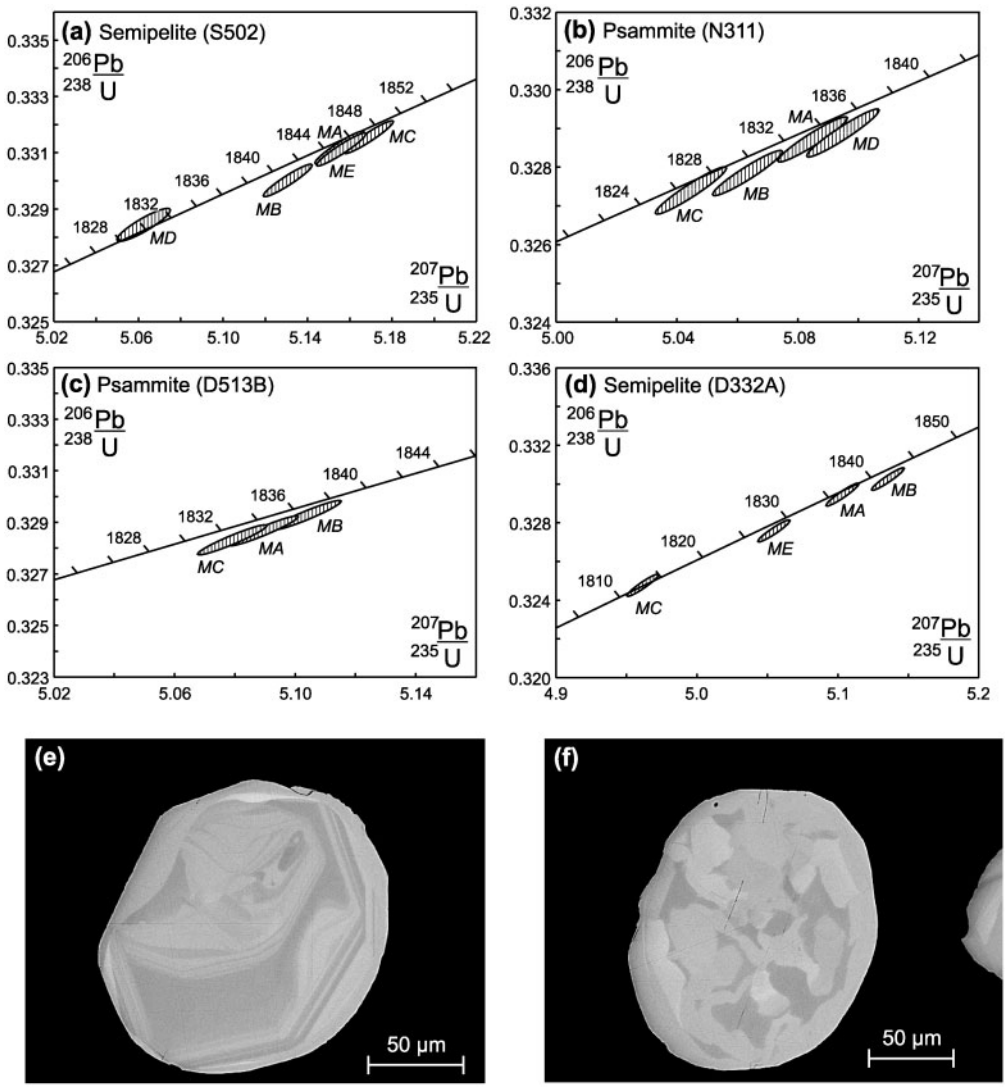


Fig. 13. (a–d) U–Pb concordia diagrams for monazite from semipelitic and psammitic rocks of the Lake Harbour Group: (a) semipelite sample S502; (b) psammite sample N311; (c) psammite sample D513B; (d) semipelite sample D332A. Error ellipses represent 2σ. (e, f) BSE images of selected monazite crystals from semipelite sample D332A: (e) monazite crystal with euhedral faces exhibiting a partly disturbed oscillatory-zoned centre surrounded by a thin homogeneous overgrowth; (f) round monazite crystal showing a patchy-zoned central domain surrounded by a thin homogeneous overgrowth.

single prismatic crystal (MD) that is somewhat reversely discordant with a $^{207}Pb/^{235}U$ age of 1830 ± 2 Ma. Whereas the older monazite group records the time of M_{1a} metamorphism at *ca.* 1849–1844 Ma (Table 8), the younger age of *ca.* 1830 Ma is attributed to a subsequent disturbance distinctly post-M_{1a} but pre-M_2 (discussed below).

Sample N311 (Fig. 5) is a foliated ($S_{1a} + S_2$) grey psammite containing large (8 mm) S_{1a} garnet poikiloblasts. Four, unabraded, single-grain fractions (MA–MD, Fig. 13b) of monazite yield near-concordant (0·1–0·3%) $^{207}Pb/^{206}Pb$ ages ranging from 1838 ± 2 to 1828 ± 2 Ma (Electronic Appendix 1). We interpret 1838 ± 2 Ma as the minimum age for monazite growth during M_{1a} metamorphism (Table 8), and the dispersion to younger ages in the other grains as indicative of partial recrystallization and (or) younger metamorphic overgrowth [as documented in samples N056 and S502 (above), and D332A (below)].

Sample D513B (Fig. 5) is a foliated (S_{1a}), grey biotite-garnet-bearing psammite. Three abraded monazite analyses (MA–MC, Fig. 13c) yield overlapping discordant (0·2–0·3%) $^{207}Pb/^{206}Pb$ ages of 1839 ± 2 to 1835 ± 2 Ma (Electronic Appendix 1). Based on similarities in colour, morphology, and chemistry (Electronic Appendix 1), we conclude that the analysed monazite grains define a single population with a minimum age of *ca.* 1839–1835 Ma for M_{1a} (Table 8).

Downloaded from http://petrology.oxfordjournals.org/ by guest on June 7, 2013

Sample D332A (Fig. 5) is a garnet–biotite–melt-bearing semipelite. Garnet occurs either as large, subhedral S_{1a} porphyroblasts with inclusions of quartz and opaque minerals or as small inclusion-free, euhedral S_2 grains. Four analyses, each consisting of a single unabraded monazite crystal (MA–ME, Fig. 13d), resulted in a range of concordant to near-concordant ages from 1845 ± 2 to 1813 ± 2 Ma (Electronic Appendix 1). BSE imaging documents fine oscillatory zoning in monazite grains with partial euhedral faces (Fig. 13e), suggestive of igneous growth, and patchy zoning in rounded grains (Fig. 13f). In addition, inner domains on a number of grains are truncated by homogeneous overgrowths of variable thickness (Fig. 13e and f). From these features, we interpret the oldest age, 1845 ± 2 Ma, to be the minimum age for M_{1a} monazite growth, and 1813 ± 2 Ma as the time of extensive recrystallization or new monazite growth during M_2 metamorphism (Table 8). The intermediate ages obtained for monazite fractions MA and ME (Electronic Appendix 1) might reflect partial recrystallization (or monazite overgrowth) during M_2.

Carbonate and mafic rocks, Lake Harbour Group

Two suitable samples of titanite-bearing rocks (D020 and D513A) were collected in the study area (Fig. 5). Sample D020 is a coarse-grained, diopside-bearing siliceous marble. Three of four analyses of titanite (TC–TE, Fig. 14a) fit a discordia line with an upper intercept age of 1790 ± 1 Ma (MSWD = 0·96). We interpret this age as corresponding to complete isotopic resetting of older titanite grains (or new mineral growth) during a post-M_2 thermal or fluid event (discussed below).

Sample D513A is a well-foliated (S_{1a}) metagabbro taken from the same outcrop as sample D513B (see above). Three of four multigrain fractions of titanite (TA–TD) analysed are normally discordant (0·5–0·7%) to concordant with $^{207}Pb/^{206}Pb$ ages of 1786 ± 7, 1784 ± 5, and 1778 ± 4 Ma (Fig. 14b). The other fraction (TD) is reversely discordant (−1·2%) and has an older $^{207}Pb/^{206}Pb$ age of 1796 ± 5 Ma, but plots on the same discordia line as the other three analyses. Regression through all four analyses yields an upper intercept age of 1785 ± 4 Ma (MSWD = 1·18) (Electronic Appendix 1). This age is distinctly younger than >1839–1835 Ma monazite separated from the adjacent semipelite D513B and is taken to indicate either the time of new titanite growth or isotopic resetting as a result of a post-M_2 thermal event (see below).

Felsic intrusive rocks, Meta Incognita microcontinent

A number of monzogranite to syenogranite dykes and syenite to monzonite plugs are parallel or discordant to the principal deformation fabrics that characterize the metamorphic rocks of the study area. Previous work on these intrusive units revealed at least three phases of pre- to post-D_2 dyke and plug emplacement: at *ca.* 1840, 1795–1784, and 1760 Ma (Scott, 1997; Table 8). Four additional samples of dykes and plugs were collected to further document the timing of magmatism concurrent with, and postdating, D_{1a} deformation and M_{1a} metamorphism in the study area.

Sample D534 (Fig. 5) is from an undeformed syenogranite pegmatite dyke oriented parallel to the S_{1a} compositional foliation in host psammitic rocks. The undeformed nature of the dyke is suggestive of a late S_{1a} emplacement. Data for five of the six analyses of zircon and monazite (MA–ZB, excluding fraction ZC, Fig. 14c) are collinear, and regression gives an upper intercept age of $1844 + 9/-3$ Ma (MSWD = 0·16). This age is interpreted as dating the emplacement of the pegmatite and suggests that formation of the regional S_{1a} foliation was waning by *ca.* 1844 Ma (Table 8).

Sample D532 (Fig. 5) is a monzogranite pegmatite that clearly cross-cuts the main S_{1a} compositional layering in host psammitic rocks. Analysis of three single- and multigrain fractions of zircon (ZA–ZC, Fig. 14d) and three single-grain fractions of monazite (MA–MC, Fig. 14d), all abraded, are in good agreement and suggest an emplacement age of 1833 ± 1 Ma on the basis of their weighted mean $^{207}Pb/^{206}Pb$ age (MSWD = 0·89; probability of fit = 0·49) (Electronic Appendix 1); 1833 Ma represents a minimum age for development of the S_{1a} compositional foliation in the study area (Table 8).

Sample D533 (Fig. 5) is an undeformed syenite plug intrusive into foliated (S_{1a}) orthopyroxene–biotite monzogranite of the Cumberland batholith. Five analyses (ZA–ZE, Fig. 14e) of zircon display only minor discordance (0·2–0·4%) with $^{207}Pb/^{206}Pb$ ages ranging between 1834 ± 2 and 1823 ± 2 Ma (Electronic Appendix 1). A weighted mean age of fractions ZA, ZB, and ZE (Fig. 14e) yields 1831 ± 3 Ma (MSWD = 1·8; probability of fit = 0·16). This age dates the emplacement of the syenite and is a minimum age for S_{1a} formation at this locality.

Sample N312 (Fig. 5) is from a cross-cutting, undeformed body of orthopyroxene-bearing monzonite (sample N312, Fig. 5) emplaced into the well-foliated (S_{1a}) orthogneissic basement to the Lake Harbour Group. Five analyses of strongly abraded zircon fragments (ZA1-ZA3, ZD, ZE, Fig. 14f) are −0·3 to 0·4% discordant and yield the oldest $^{207}Pb/^{206}Pb$ ages, between 1834 ± 2 and 1829 ± 2 Ma (Electronic Appendix 1). Three of the five analyses (ZA1, ZA2, and ZE, Fig. 14f) yield a weighted mean $^{207}Pb/^{206}Pb$ age of 1834 ± 1 Ma (MSWD = 0·024; probability of fit = 0·98). The remaining two analyses, including a tip (ZA3, Fig. 14f), give a slightly younger age of *ca.* 1830 Ma. One analysis of small subequant zircon grains (ZB, Fig. 14f) and two analyses of subhedral to anhedral monazite (MC and ME, Fig. 14f) define a discordia line with a distinctly younger upper intercept of $1816 + 2/-1$ Ma (MSWD = 0·54). A third analysis of

Downloaded from http://petrology.oxfordjournals.org/ by guest on June 7, 2013

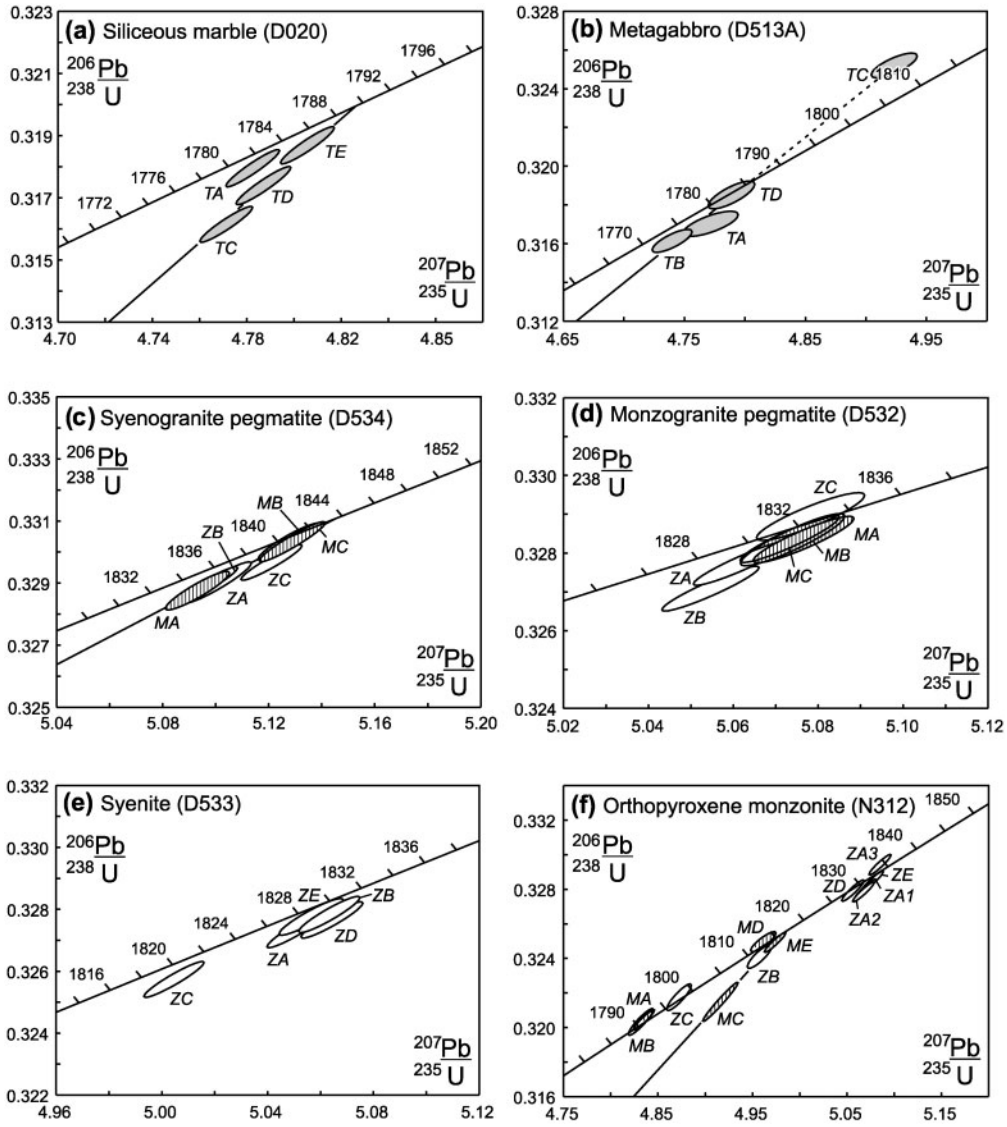


Fig. 14. (a, b) U–Pb concordia diagrams for titanite from (a) marble sample D020 and (b) metagabbro sample D513A. Error ellipses represent 2σ. (c–f) U–Pb concordia diagrams for zircon (white ellipses) and monazite (vertically ruled ellipses) from felsic intrusive rocks: (c) syenogranite pegmatite D534; (d) monzogranite pegmatite D532; (e) syenite D533; (f) orthopyroxene–biotite monzonite N312. Error ellipses represent 2σ.

subhedral monazite (MD, Fig. 14f) plots slightly above concordia but has an overlapping $^{207}Pb/^{235}U$ age of 1813 ± 2 Ma. A small zircon prism (ZC, Fig. 14f) is concordant at 1797 ± 2 Ma. Finally, the two youngest analyses of euhedral monazite (MA and MB, Fig. 14f) give a weighted mean $^{207}Pb/^{235}U$ age of 1791 ± 2 Ma. These results, combined with textural and chemical inhomogeneities of the analysed zircon and monazite populations (Electronic Appendix 1), provide evidence for multiple mineral growth events. The external morphology of the oldest zircon grains (Electronic Appendix 1) is consistent with a magmatic origin at 1834 ± 1 Ma. This result places a minimum age on S_{1a} foliation formation. The slightly younger *ca.* 1830 Ma age may indicate the time of granulite-facies metamorphism of the monzonite, shortly following its crystallization. The younger 1816 + 2/−1 Ma, 1797 ± 2 Ma, and 1791 ± 2 Ma ages are interpreted to reflect episodic (or prolonged) zircon and monazite growth during and following M_2 regional metamorphism as a result of mainly retrograde fluid flow (discussed below).

DISCUSSION

The integration of mineral growth–deformation fabric relationships, thermobarometric results, and petrological data provided by representative phase diagrams allows

Downloaded from http://petrology.oxfordjournals.org/ by guest on June 7, 2013

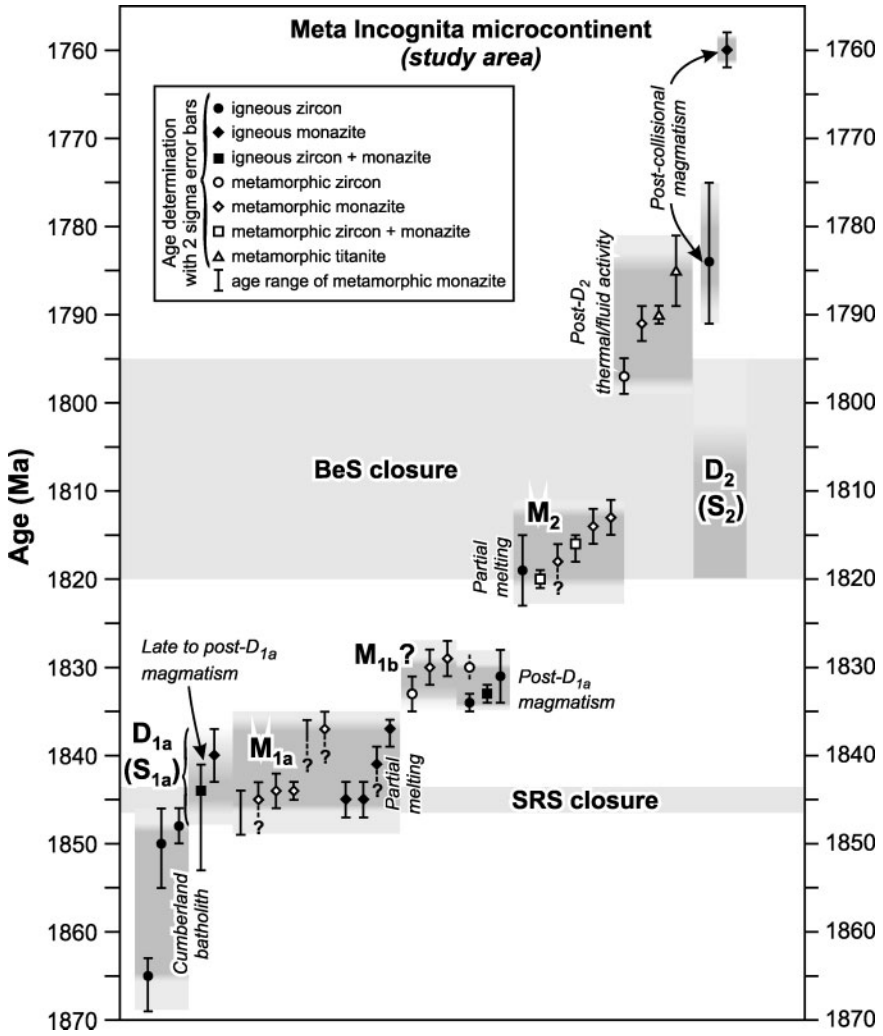


Fig. 15. Summary of available U–Pb ages for the main magmatic, deformation and metamorphic events in the southern Baffin Island study area. Only the most precise U–Pb ages (i.e. with errors less than ± 10 Ma) are plotted. (See text for sources of data and discussion.) BeS, Bergeron suture; SRS, Soper River suture.

the identification and characterization of two contrasting, regionally significant, tectono-metamorphic events (M_{1a}, M_2) in the internal zone of the Trans-Hudson Orogen. New U–Pb data document the timing and duration of these two metamorphic events, allow the reinterpretation of previously acquired age data for the study area, and reveal additional complexities in the polymetamorphic evolution of southern Baffin Island. In this section, we summarize the main results and identify the potential causes of metamorphism for each thermal event documented in the study area, and draw parallels with the thermal evolution of the upper-plate domain in the Cenozoic India–Asia collision zone.

M_{1a} metamorphism

The oldest regional metamorphic event identified by this study, M_{1a}, is characterized by granulite-facies assemblages in metapelite and is associated with the development of a pervasive compositional foliation (S_{1a}) in the metamorphic rocks of southern Baffin Island (petrology samples D515, S502, M500, P501, and S501; XRF sample N016). S_{1a} assemblages reflect P–T conditions of up to 810°C and 8·3 kbar (Table 7), and evolved along a steep, compressional P–T path segment (Figs 8 and 9). U–Pb ages from metamorphic monazite in siliciclastic units with pervasive S_{1a} assemblages and fabrics (geochronology samples D513B, D332A, N311, and S502) indicate monazite growth between *ca.* 1849 and 1835 Ma (Fig. 15). These new data indicate that high-grade M_{1a} metamorphic conditions were maintained for at least 14 Myr, during which time the S_{1a} assemblages and foliation were developed (Fig. 15), and are consistent with previously reported ages for metamorphic monazite from other siliciclastic

Downloaded from http://petrology.oxfordjournals.org/ by guest on June 7, 2013

samples of the Meta Incognita microcontinent (see Table 8; Wodicka & Scott, 1997).

New dating of anatectic granites (geochronology samples D094B and N056) bracket partial melting at before *ca.* 1841–1837 Ma (Table 8). These results are consistent with two previously reported 1845 ± 2 Ma age determinations (Scott, 1997; Wodicka & Scott, 1997) for monzogranitic melt pods and veins in the study area. The results highlight the intimate field and temporal association that can be established between granulite-facies garnet–cordierite (M_{1a}) metamorphism, anatexis, and regional (S_{1a}) foliation development in the study area.

The *ca.* 1849–1835 Ma age span determined for M_{1a} metamorphism and partial melting partly coincides with the waning stages of *ca.* 1865–1848 Ma Cumberland batholith magmatism (Jackson *et al.*, 1990; Wodicka & Scott, 1997; Scott & Wodicka, 1998; Scott, 1999; Fig. 15) and largely postdates the timing of accretion of the intra-oceanic Narsajuaq arc to the leading edge of the upper (Churchill) plate (i.e. the study area, Fig. 4c) at *ca.* 1845 Ma (see above). We therefore propose that the M_{1a} regional metamorphic event and associated partial melting was caused not only by emplacement of the Andean-type Cumberland batholith, which probably played a significant role in the attainment of peak M_{1a} metamorphic conditions in an upper-plate setting (e.g. Wodicka & St-Onge, 1998; St-Onge *et al.*, 2000b), but also by the crustal thickening (D_{1a}) related to the collision and accretion of the Narsajuaq arc to the southern margin of the Meta Incognita microcontinent (and manifest in the study area as S_{1a}) at *ca.* 1845 Ma.

Late- to post-D_{1a} crustal magmatism, S_{1a} foliation formation, and M_{1b} metamorphism

U–Pb data from four felsic dykes and plugs (geochronology samples D532, D533, D534, and N312) constrain the age of late- to post-accretion (D_{1a}) crustal magmatism and S_{1a} foliation formation. The oldest dyke (D534), dated at 1844 + 9/–3 Ma (Table 8), was largely coeval with M_{1a} metamorphism, being emplaced during a late stage of S_{1a} foliation development (Fig. 15). A similar, late to post-S_{1a} monzogranite dyke was dated by Scott (1997) at 1840 ± 3 Ma (Table 8). In contrast, a distinctly younger phase of felsic crustal magmatism, dominated by undeformed dykes and plugs (geochronology samples D532, D533, and N312), took place at *ca.* 1834–1831 Ma. Field observations indicate that these younger intrusive rocks cut the well-developed S_{1a} foliation on southern Baffin Island. Thus, the intrusion ages and structural state of individual dykes and plugs indicate that development of S_{1a} in the southern Baffin Island study area occurred mostly prior to *ca.* 1844–1840 Ma and must have ended before *ca.* 1834–1831 Ma. These age determinations indicate that S_{1a} foliation formation was largely coeval with D_{1a} accretion of the Narsajuaq arc at *ca.* 1845 Ma, and may therefore be related to closure of the Soper River suture (Fig. 15) and consequent Andean-type tectonic thickening along the southern margin of the Meta Incognita microcontinent.

A concordant 1830 ± 2 Ma age from metamorphic monazite in sample S502, as well as previously published monazite and zircon data by Scott & Gauthier (1996), Wodicka & Scott (1997), and Scott & Wodicka (1998) (Table 8) suggest that rocks from southern Baffin Island experienced a thermal perturbation at *ca.* 1833–1829 Ma. Whether these ages reflect continued mineral growth during the waning stages of a protracted M_{1a} metamorphic event, or whether they represent a distinct thermal event (M_{1b}; Fig. 15) related to intrusion of the *ca.* 1834–1831 Ma felsic dykes and plugs remains uncertain. The latter hypothesis is favoured by: (1) evidence for two distinct episodes of monazite growth in sample S502 at *ca.* 1849–1844 Ma and at 1830 ± 2 Ma (Table 8); (2) the presence of *ca.* 1830 Ma metamorphic zircon in monzonite sample N312; and (3) the post-S_{1a} character of the 1834–1831 Ma magmatic suite. Regardless of the interpretation, the combined data imply that temperatures in the study area remained high for at least 20 Myr, from about 1849 until 1829 Ma.

M_2 metamorphism

The second regional metamorphic event, M_2, is characterized by the growth of upper amphibolite-facies assemblages at the expense of S_{1a} assemblages, the development of a penetrative, schistose, sub-millimetre-scale S_2 foliation, and the growth of sparse, sub-equant S_2 garnets that are generally aligned with, and overgrow, the schistose foliation (petrology samples D518, D527, E501, J501, N516, M500, P501, and S501; XRF sample D024). S_2 metapelitic assemblages record a clockwise, decompression *P–T* path segment (Figs 10 and 11) and *P–T* conditions during M_2 are estimated as having involved 710°C and 6·0 kbar from mineral rim compositions (Table 7). New concordant monazite ages for siliciclastic and anatectic granite units (geochronology samples D332A and N056) bracket the retrograde M_2 metamorphic event between *ca.* 1820 and 1813 Ma (Table 8). Effects of M_2 are also recorded by new growth and (or) recrystallization of monazite or zircon in geochronology samples N056, D094B, and N312 (Table 8). The *ca.* 1820–1813 Ma ages overlap with previously reported *ca.* 1819–1814 Ma metamorphic zircon and monazite ages for the Lake Harbour Group and Blandford Bay assemblage (Wodicka & Scott, 1997; Scott *et al.*, 2002).

The clockwise decompressive *P–T* path segment documented for M_2 is consistent with numerical models for the thermal evolution of tectonically thickened crust (e.g. England & Thompson, 1984), and the *ca.* 1820–1813 Ma age span for M_2 closely corresponds to the early stages of D_2 collision in Trans-Hudson

Downloaded from http://petrology.oxfordjournals.org/ by guest on June 7, 2013

Orogen (bracketed between *ca.* 1820 and 1795 Ma; Wodicka & Scott, 1997; Scott & Wodicka, 1998; Fig. 15). Growth of the S_2 assemblages in the study area appears to be closely tied to the intensity of foliation development (Table 1) whereas U–Pb data presented in Electronic Appendix 1, and summarized above, strongly suggest that the D_2 event had an influence on the U–Pb systematics of monazite and zircon. In general, greatest recrystallization by S_2 mineral assemblages, including new growth and (or) recrystallization of monazite or zircon, occurs in samples that exhibit a strong penetrative foliation and are located in the immediate vicinity of D_2 thrusts (e.g. petrology samples D518, D527, E501, J501, N516; geochronology samples N056, D332A, and D094B). Thus, deformation-enhanced fluid circulation during retrograde amphibolite-facies metamorphism (e.g. St-Onge *et al.*, 2000*b*) directly related to the D_2 collision of the upper (Churchill) plate (i.e. including the study area) with the lower-plate Superior craton (Fig. 4e) appears to have been instrumental in promoting partial to total recrystallization and new growth of M_2 silicate assemblages, monazite, and zircon in the polymetamorphic rocks of southern Baffin Island.

Post-D_2 thermal and fluid activity

Two lines of evidence suggest that the youngest zircon, monazite, and titanite ages of *ca.* 1797–1785 Ma from the study area (geochronology samples D020, D513A, N312; Table 8) might be related to post-collisional thermal activity or fluid infiltration rather than to cooling. First, the *ca.* 1797–1785 Ma age range overlaps in time with emplacement of *ca.* 1795–1784 Ma post-collisional syenogranite pegmatite dykes in the composite upper (Churchill) plate (Scott, 1997; Wodicka & Scott, 1997; Fig. 15). Second, late fluid infiltration would be consistent with petrographic evidence for minor greenschist-facies retrogression, which includes secondary chlorite, muscovite, and epidote spatially associated with fractures and sericitized plagioclase noted in, for example, sample N312.

Upper-plate magmatism and metamorphism in the India–Asia collison zone

In the western upper-plate (Asian) domain of the Cenozoic India–Asia collision zone, the Karakoram batholith includes a series of pre-collisional deformed and metamorphosed 150–95 Ma granitoids (Searle *et al.*, 1989, 1990; Treolar *et al.*, 1989; Searle, 1991; Crawford & Searle, 1992; Fraser *et al.*, 2001; Hildebrand *et al.*, 2001), as well as massive, pre-collisional, mid-Cretaceous, I-type plutonic suites (Fraser *et al.*, 2001). The younger Transhimalayan batholith (Singh & Jain, 2003) is a linear belt of Andean-type plutons that extends the full length of the exposed upper plate and is bracketed between 102 ± 2 Ma and $49{\cdot}8 \pm 0{\cdot}8$ Ma (Scharer *et al.*, 1984; Weinberg & Dunlap, 2000). Taken as a set, these Andean-type plutonic units witness the long-lived nature of the upper-plate margin of Asia, with most magmatic units probably formed above pre-collisional northward-directed subduction zones prior to the India–Asia collision (Searle *et al.*, 1999).

Several episodes of high-grade, regional, Barrovian metamorphism are documented in the Karakoram upper-plate domain (Searle & Tirrul, 1991; Fraser *et al.*, 2001; Hildebrand *et al.*, 2001). U–Pb monazite ages from staurolite-grade schists and sillimanite-grade gneisses pre-dating the India–Asia collision peak at *ca.* 135–126, 106–102 and $82{\cdot}9 \pm 6{\cdot}1$ to $61{\cdot}9 \pm 4{\cdot}7$ Ma (Fraser *et al.*, 2001; Hildebrand *et al.*, 2001). Metamorphism postdating the collision event is dated at 44, 28, 16, and 5 Ma (Fraser *et al.*, 2001). The youngest dated metamorphism is a high-temperature, sillimanite-grade partial melting event in the core of a metamorphic core complex along the southern Karakoram (Dassu gneiss at $5{\cdot}4 \pm 0{\cdot}2$ Ma; Fraser *et al.*, 2001), a metamorphism that is probably still continuing today at depth (Searle, 2007).

We surmise that the polymetamorphic evolution documented for the internal zone of the Trans-Hudson Orogen on southern Baffin Island (this study) and that documented for the upper-plate domain of the India–Asia collision zone (Searle, 2007; and references therein) are analogous in type, duration, and extent. In both orogens, early upper-plate thermal events are interpreted as driven by heat advection related to the emplacement of pre-collision, Andean-type plutonic suites, whereas subsequent metamorphic events are related to either the continental collision itself or to post-collisional crustal fluid flow.

CONCLUSIONS

The integration of new structural, metamorphic, and geochronological data and observations from the southern Baffin Island study area document that metasedimentary and metaplutonic rocks from the internal zone of the Trans-Hudson Orogen record a complex plate-margin to intraplate polymetamorphic history that includes the following events.

(1) Three deformation events (D_0, D_{1a}, D_2), which are the result of the sequential north to south closing of three crustal sutures (the Baffin suture, Soper River suture, and Bergeron suture).

(2) A granulite-facies regional metamorphic event (M_{1a}) that is characterized by an approximately isothermal, compressive P–T path segment and the development of a dominant (S_{1a}) compositional foliation. M_{1a} is associated with the emplacement of a pre-collision, Andean-type magmatic batholith and crustal

Downloaded from http://petrology.oxfordjournals.org/ by guest on June 7, 2013

thickening related to the accretion of an intra-oceanic arc to the evolving upper plate.

(3) A retrograde regional metamorphic event (M_2), which is characterized by a clockwise, decompression P–T path segment and the development of a penetrative schistose S_2 foliation. M_2 is associated with crustal deformation and fluid infiltration generated by continent–continent collision.

(4) At least two localized thermal events (M_{1b}, post-D_2), associated with post-accretion and post-collision crustal magmatism.

The protracted (*ca.* 80 Myr) record of magmatism, deformation, and metamorphism documented for the internal zone of Trans-Hudson Orogen on Baffin Island reveals a Paleoproterozoic tectonothermal evolution, which is similar in character, scope, and scale to that of the upper plate of other, younger orogenic belts, in particular that of the Himalaya–Karakoram Orogen of Asia (e.g. Hildebrand *et al.*, 2001*l*; Fraser *et al.*, 2001). We suggest that the results presented in this study provide tangible evidence for the operation of modern plate-margin to intraplate tectonometamorphic processes back to the early Paleoproterozoic.

SUPPLEMENTARY DATA

Supplementary data for this paper are available at *Journal of Petrology* online.

ACKNOWLEDGEMENTS

Samples utilized in this study were collected during a Geological Survey of Canada (GSC) project in the southern Baffin Island region led by the first author. Discussions with Rob Berman (GSC), David Corrigan (GSC), and Dave Scott (GSC) are gratefully acknowledged. We thank the technical staff at the GSC Geochronology and Scanning Electron Microscopy laboratories for their help with U–Pb analytical work and SEM imaging, and Rob Berman for his assistance in producing the two petrological phase diagrams. Helpful and thorough reviews of earlier versions of this paper were provided by Rob Berman, Geoffrey Clarke, David Corrigan, Dave Kelsey, and one anonymous reviewer. The Polar Continental Shelf Project is acknowledged for its generous helicopter and Twin Otter support during the course of the fieldwork. This paper is ESS Contribution 20050411.

REFERENCES

Berman, R. G. (1988). Internally-consistent thermodynamic data for stoichiometric minerals in the system Na_2O–K_2O–CaO–MgO–FeO–Fe_2O_3–Al_2O_3–SiO_2–TiO_2–H_2O–CO_2. *Journal of Petrology* **29**, 445–522.

Berman, R. G. (1991). Thermobarometry using multi-equilibrium calculations: a new technique, with petrological applications. *Canadian Mineralogist* **29**, 833–855.

Berman, R. G. & Aranovich, L. Y. (1996). Optimized standard state and mixing properties of minerals: I. Model calibration for olivine, orthopyroxene, cordierite, garnet, and ilmenite in the system FeO–MgO–CaO–Al_2O_3–SiO_2–TiO_2. *Contributions to Mineralogy and Petrology* **126**, 1–24.

Bethune, K. M. & Scammel, R. J. (2003). Geology, geochronology, and geochemistry of Archean rocks in the Eqe Bay area, north–central Baffin Island, Canada: constraints on the depositional and tectonic history of the Mary River Group of northeastern Rae Province. *Canadian Journal of Earth Sciences* **40**, 1137–1167.

Carr, S. D., Easton, R. M., Jamieson, R. A. & Culshaw, N. G. (2000). Geological transect across the Grenville orogen of Ontario and New York. *Canadian Journal of Earth Sciences* **37**, 193–216.

Crawford, M. B. & Searle, M. P. (1992). Field relationships and geochemistry of pre-collisional (India–Asia) granitoid magmatism in the central Karakoram, northern Pakistan. *Tectonophysics* **206**, 171–192.

Culshaw, N. G., Jamieson, R. A., Ketchum, J. W. F., Wodicka, N., Corrigan, D. & Reynolds, P. H. (1997). Transect across the northwestern Grenville orogen, Georgian Bay, Ontario: Polystage convergence and extension in the lower orogenic crust. *Tectonics* **16**, 966–982.

Davis, W. J., McNicoll, V. J., Bellerive, D. R., Santowski, K. & Scott, D. J. (1997). Modified chemical procedures for the extraction and purification of U from titanite, allanite, and rutile in the Geochronology Laboratory, Geological Survey of Canada*Radiogenic Age and Isotopic Studies: Report 10; Geological Survey of Canada, Current Research* **1997-F**, 33–35.

Davis, W. J., Parrish, R. R., McNicoll, V. & Bellerive, D. (1998). Analytical techniques for the determination of $^{208}Pb/^{232}Th$ ages of monazite and zircon at the Geochronology Laboratory, Geological Survey of Canada. In: *Radiogenic Age and Isotopic Studies: Report 11; Geological Survey of Canada, Current Research* **1998-F**, 19–22.

De Capitani, C. (1994). Gleichgewichts-Phasendiagramme: Theorie und Software. *Berichte der Deutschen Mineralogischen Gesellschaft* **72**, 14.

Dunphy, J. M. & Ludden, J. N. (1998). Petrological and geochemical characteristics of a Paleoproterozoic magmatic arc (Narsajuaq Terrane, Ungava Orogen, Canada) and comparisons to Superior Province granitoids. *Precambrian Research* **91**, 109–142.

England, P. C. & Thompson, A. B. (1984). Pressure–temperature–time paths of regional metamorphism. I. Heat transfer during the evolution of regions of thickened continental crust. *Journal of Petrology* **25**, 894–928.

Essene, E. J. (1989). The current status of thermobarometry in metamorphic rocks. In: Daly, J. S., Cliff, R. A. & Yardley, B. W. D. (eds) *Evolution of Metamorphic Belts. Geological Society, London, Special Publications* **43**, 1–44.

Foster, G., Gibson, H. D., Parrish, R., Horstwood, M., Fraser, J. & Tindle, A. (2002). Textural, chemical and isotopic insights into the nature and behaviour of metamorphic monazite. *Chemical Geology* **191**, 183–207.

Fraser, J. E., Searle, M. P., Parrish, R. R. & Noble, S. R. (2001). Chronology of deformation, metamorphism, and magmatism in the southern Karakoram Mountains. *Geological Society of America Bulletin* **113**, 1443–1455.

Harrison, T. M., Ryerson, F. J., Le Fort, P., An Yin, , Lovera, O. M. & Catlos, E. J. (1997). A late Miocene–Pliocene origin for the Central Himalayan inverted metamorphism. *Earth and Planetary Science Letters* **146**, E1–E7.

Downloaded from http://petrology.oxfordjournals.org/ by guest on June 7, 2013

Hildebrand, P. R., Noble, S. R., Searle, M. P., Waters, D. J. & Parrish, R. R. (2001). Old origin for an active mountain range: geology and geochronology of the eastern Hindu Kush, Pakistan. *Geological Society of America Bulletin* **113**, 625–639.

Hoffman, P. F. (1988). United Plates of America, the birth of a craton: Early Proterozoic assembly and growth of Laurentia. *Annual Review of Earth and Planetary Sciences* **16**, 543–603.

Holland, T. J. B. & Powell, R. (1998). An internally consistent thermodynamic data set for phases of petrological interest. *Journal of Metamorphic Geology* **16**, 309–343.

Huerta, A. D., Royden, L. H. & Hodges, K. V. (1998). The thermal structure of collisional orogens as a response to accretion, erosion, and radiogenic heating. *Journal of Geophysical Research* **103**, 15287–15302.

Huerta, A. D., Royden, L. H. & Hodges, K. V. (1999). The effects of accretion, erosion and radiogenic heat on the metamorphic evolution of collisional orogens. *Journal of Metamorphic Geology* **17**, 349–366.

Indares, A., Dunning, G. & Cox, R. (2000). Tectono thermal evolution of deep crust in a Mesoproterozoic continental collision setting: the Manicouagan example. *Canadian Journal of Earth Sciences* **37**, 325–340.

Jackson, G. D. (1969). Reconnaissance of north–central Baffin Island. *Geological Survey of Canada Paper* **69-1**, 171–176.

Jackson, G. D. (2000). *Geology of the Clyde–Cockburn Land Map Area, North–Central Baffin Island, Nunavut. Geological Survey of Canada Memoir* **440**, 303 pp.

Jackson, G. D. (2002). Geology, Isurtuq River–Nedlukseak Fiord, Nunavut. *Geological Survey of Canada Open File Map* **4259**, scale 1:250 000.

Jackson, G. D., Hunt, P. A., Loveridge, W. D. & Parrish, R. R. (1990). Reconnaissance geochronology of Baffin Island, N. W. T. *Geological Survey of Canada Paper* **89-2**, 123–148.

Jamieson, R. A., Culshaw, N. G. & Corrigan, D. (1995). North-west propagation of the Grenville orogen: Grenvillian structure and metamorphism near Key Harbour, Georgian Bay, Ontario, Canada. *Journal of Metamorphic Geology* **13**, 185–207.

Jamieson, R. A., Beaumont, C., Hamilton, J. & Fullsack, P. (1996). Tectonic assembly of inverted metamorphic sequences. *Geology* **24**, 839–842.

Jamieson, R. A., Beaumont, C., Fullsack, P. & Lee, B. (1998). Barrovian regional metamorphism: where's the heat? In: Treloar, P. J. & O'Brien, P. (eds) *What Drives Metamorphism and Metamorphic reactions? Geological Society, London, Special Publications* **138**, 23–45.

Jamieson, R. A., Beaumont, C., Ngyen, M. H. & Lee, B. (2002). Interaction of metamorphism, deformation and exhumation in large convergent orogens. *Journal of Metamorphic Geology* **20**, 9–24.

Johnson, T. E., Brown, M. & Solar, G. S. (2003). Low-pressure subsolidus and suprasolidus phase equilibria in the MnNCKFMASH system: constraints on conditions of regional metamorphism in western Maine, northern Appalachians. *American Mineralogist* **88**, 624–638.

Kretz, R. (1983). Symbols for rock-forming minerals. *American Mineralogist* **68**, 277–279.

Krogh, T. E. (1982). Improved accuracy of U–Pb ages by creation of more concordant systems using an air abrasion technique. *Geochimica et Cosmochimica Acta* **46**, 637–649.

Krogh, T. E. & Davis, G. L. (1973). The effect of regional metamorphism on U–Pb systems in zircon and comparison with Rb–Sr systems in the same whole rock. *Carnegie Institution of Washington Yearbook* **72**, 601–610.

Lewry, J. F. & Collerson, K. D. (1990). The Trans-Hudson Orogen; extent, subdivisions, and problems. In: Lewry, J. F. & Stauffer, M. R. (eds) *The Early Proterozoic Trans-Hudson Orogen of North America. Geological Association of Canada, Special Papers* **37**, 1–14.

Lucas, S. B. (1989). Structural evolution of the Cape Smith Thrust Belt and the role of out-of-sequence faulting in the thickening of mountain belts. *Tectonics* **8**, 655–676.

Ludwig, K. R. (2003). *Isoplot/Ex Version 3.00: a Geochronological Toolkit for Microsoft Excel. Berkeley Geochronology Center Special Publications* **4**, 70 pp.

Machado, N., David, J., Scott, D. J., Lamothe, D., Philippe, S. & Gariépy, C. (1993). U–Pb geochronology of the western Cape Smith Belt, Canada: new insights on the age of initial rifting and arc magmatism. *Precambrian Research* **63**, 211–223.

Marmo, B. A., Clarke, G. L. & Powell, R. (2002). Fractionation of bulk rock composition due to porphyroblast growth: effects on eclogite facies mineral equilibria, Pam Peninsula, New Caledonia. *Journal of Metamorphic Geology* **20**, 151–165.

Moecher, D. P. (1999). The distribution, style and intensity of Alleghanian metamorphism in south–central New England: petrologic evidence from the Pelham and Willimantic Domes. *Journal of Geology* **107**, 449–471.

Parrish, R. R. (1989). U–Pb geochronology of the Cape Smith belt and Sugluk block. *Geoscience Canada* **16**, 126–130.

Parrish, R. R., Roddick, J. C., Loveridge, W. D. & Sullivan, R. W. (1987). Uranium–lead analytical techniques at the Geochronology Laboratory, Geological Survey of Canada. In: *Radiogenic Age and Isotopic Studies: Report 1; Geological Survey of Canada Paper* **87-2**, 3–7.

Pouchou, J. L. & Pichoir, F. (1984). A new model for quantitative X-ray microanalysis. *Recherche Aerospatiale* **3**, 167–192.

Roddick, J. C. (1987). Generalized numerical error analysis with applications to geochronology and thermodynamics. *Geochimica et Cosmochimica Acta* **51**, 2129–2135.

Rowley, D. B., Currie, B. S., Kidd, W. S. F. & Zhu, B. (2004). India–Asia collision and Himalaya–Tibet orogenesis sensu stricto. *Geological Society of America, Abstracts with Programs* **36**, 408.

Scharer, U., Xu, R. H. & Allègre, C. J. (1984). U–Pb geochronology of Gandase Transhimalyan plutonism in the Lahasa–Xigaze region, Tibet. *Earth and Planetary Sciences Letters* **69**, 311–320.

Scott, D. J. (1997). Geology, U–Pb, and Pb–Pb geochronology of the Lake Harbour area, southern Baffin Island: implications for the Paleoproterozoic tectonic evolution of north-eastern Laurentia. *Canadian Journal of Earth Sciences* **34**, 140–155.

Scott, D. J. (1998). U–Pb ages of Archean crust in the southeast arm of the Rae Province, southeastern Ungava Bay, Quebec. *Geological Survey of Canada Paper* **1998-F**, 41–45.

Scott, D. J. (1999). U–Pb geochronology of the eastern Hall Peninsula, southern Baffin Island, Canada: a northern link between the Archean of West Greenland and the Paleoproterozoic Torngat orogen of northern Labrador. *Precambrian Research* **93**, 5–26.

Scott, D. J. & Gauthier, G. (1996). Comparison of TIMS (U–Pb) and laser ablation microprobe ICP-MS (Pb) techniques for age determination of detrital zircons from Paleoproterozoic metasedimentary rocks from northeastern Laurentia, Canada, with tectonic implications. *Chemical Geology* **131**, 127–142.

Scott, D. J. & St-Onge, M. R. (1995). Constraints on Pb closure temperature in titanite based on rocks from the Ungava orogen, Canada: implications for U–Pb geochronology and P–T–t path determinations. *Geology* **23**, 1123–1126.

Scott, D. J. & Wodicka, N. (1998). A second report on the U–Pb geochronology of southern Baffin Island. *Geological Survey of Canada Paper* **1998-F**, 47–57.

Downloaded from http://petrology.oxfordjournals.org/ by guest on June 7, 2013

Scott, D. J., St-Onge, M. R., Wodicka, N. & Hanmer, S. (1997). Geology of the Markham Bay–Crooks Inlet area, southern Baffin Island, Northwest Territories. *Geological Survey of Canada Paper* **1997-C**, 157–166.

Scott, D. J., Stern, R. A., St-Onge, M. R. & McMullen, S. M. (2002). U–Pb geochronology of detrital zircons in metasedimentary rocks from southern Baffin Island: implications for the Paleoproterozoic tectonic evolution of Northeastern Laurentia. *Canadian Journal of Earth Sciences* **39**, 611–623.

Scott, D. J., St-Onge, M. R. & Corrigan, D. (2003). *Geology of the Archean Rae Craton and Mary River Group and the Paleoproterozoic Piling Group, Central Baffin Island, Nunavut. Geological Survey of Canada Paper* **2003-C26**, 12 pp.

Searle, M. P. (1991). *Geology and Tectonics of the Karakoram Mountains*. Chichester: John Wiley, 358 pp.

Searle, M. P. (2007). Diagnostic features and processes in the construction and evolution of Oman, Zagros, Himalayan, Karakoram and Tibetan-type orogenic belts. In: *Geological Society of America, Special Papers* (in press).

Searle, M. P. & St-Onge, M. R. (2004). The Trans-Hudson Orogen of North America and the Himalaya–Karakoram–Tibetan Orogen of Asia, Part 2: Structural and thermal evolution of the upper plate. *Geological Society of America, Abstracts with Programs* **36**, 408.

Searle, M. P. & Tirrul, R. (1991). Structural and thermal evolution of the Karakoram crust, *Journal of the Geological Society, London* **148**, 65–82.

Searle, M. P., Rex, A. J., Tirrul, R., Rex, D. C. & Barnicoat, A. (1989). Metamorphic, magmatic and tectonic evolution of the central Karakoram in the Biafo–Baltoro–Hushe regions of north Pakistan. In: Melinconico, L. L. Jr. & Lillie, R. G. (eds) *Tectonics of the Western Himalayas. Geological Society of America, Special Papers* **232**, 47–74.

Searle, M. P., Parrish, R. R., Tirrul, R. & Rex, D. C. (1990). Age of crystallization and cooling of the K2 gneiss in the Baltoro Karakoram. *Journal of the Geological Society, London* **147**, 603–606.

Searle, M. P., Asif Khan, M., Fraser, J. E. & Gough, S. J. (1999). The tectonic evolution of the Kohistan–Karakoram collision belt along the Karakoram Highway transect, north Pakistan. *Tectonics* **18**, 929–949.

Searle, M. P., Simpson, R. L., Law, R. D., Parrish, R. R. & Waters, D. J. (2003). The structural geometry, metamorphic and magmatic evolution of the Everest massif, High Himalaya of Nepal–South Tibet. *Journal of the Geological Society, London* **160**, 345–366.

Singh, S. & Jain, A. K. (2003). Himalayan granitoids. In: Singh, S. (ed.) *Granitoids of the Himalayan Collisional Belt*. Virtual Explorer, Electronic Edition, v. 11, Paper 01.

Spear, F. S. (1993). *Metamorphic Phase Equilibria and Pressure–Temperature–Time Paths*. Washington, DC: Mineralogical Society of America.

Steiger, R. H. & Jäger, E. (1977). Subcommission on geochronology: convention on the use of decay constants in geo- and cosmochronology. *Earth and Planetary Science Letters* **36**, 359–362.

Stern, R. A. & Sanborn, N. (1998). Monazite U–Pb and Th–Pb geochronology by high-resolution secondary ion mass spectrometry. *Geological Survey of Canada Paper* **1998-F**, 1–18.

St-Onge, M. R. (1984). Geothermometry and geobarometry in pelitic rocks of north–central Wopmay Orogen (early Proterozoic), Northwest Territories, Canada. *Geological Society of America Bulletin* **95**, 196–208.

St-Onge, M. R. & Ijewliw, O. J. (1996). Mineral corona formation during high-*P* retrogression of granulitic rocks, Ungava Orogen, Canada. *Journal of Petrology* **37**, 553–582.

St-Onge, M. R. & Searle, M. P. (2004). The Trans-Hudson Orogen of North America and the Himalayan Orogen of Asia, Part 1: Structural and thermal evolution of the lower plate. *Geological Society of America, Abstracts with Programs* **36**, 408.

St-Onge, M. R., Lucas, S. B. & Parrish, R. R. (1992). Terrane accretion in the internal zone of the Ungava orogen, northern Quebec: Part 1. Tectonostratigraphic assemblages and their tectonic implications. *Canadian Journal of Earth Sciences* **29**, 746–764.

St-Onge, M. R., Hanmer, S. & Scott, D. J. (1996). Geology of the Meta Incognita Peninsula, south Baffin Island: tectonostratigraphic units and regional correlations. *Geological Survey of Canada Paper* **1996-C**, 63–72.

St-Onge, M. R., Lucas, S. B., Scott, D. J. & Wodicka, N. (1999*a*). Upper and lower plate juxtaposition, deformation and metamorphism during crustal convergence, Trans-Hudson Orogen (Quebec–Baffin segment), Canada. *Precambrian Research* **93**, 27–49.

St-Onge, M. R., Scott, D. J. & Wodicka, N. (1999*b*). Geological maps and descriptive notes and legend, parts of Meta Incognita Peninsula, Nunavut. *Geological Survey of Canada Maps* **1979A to 1985A**, scale 1:100 000.

St-Onge, M. R., Scott, D. J. & Lucas, S. B. (2000*a*). Early partitioning of Quebec: microcontinent formation in the Paleoproterozoic. *Geology* **28**, 323–326.

St-Onge, M. R., Wodicka, N. & Lucas, S. B. (2000*b*). Granulite- and amphibolite-facies metamorphism in a convergent-plate-margin setting: synthesis of the Quebec–Baffin segment of the Trans-Hudson Orogen. *Canadian Mineralogist* **38**, 379–398.

St-Onge, M. R., Scott, D. J. & Wodicka, N. (2001). Terrane boundaries within Trans-Hudson Orogen (Quebec–Baffin segment), Canada: changing structural and metamorphic character from foreland to hinterland. *Precambrian Research* **107**, 75–91.

St-Onge, M. R., Scott, D. J. & Wodicka, N. (2002). Review of crustal architecture and evolution in the Ungava Peninsula–Baffin Island area: connection to the Lithoprobe ECSOOT transect. *Canadian Journal of Earth Sciences* **39**, 589–610.

St-Onge, M. R., Wodicka, N. & Searle, M. (2005*a*). The Trans-Hudson Orogen of North America and the Himalayan–Karakoram–Tibetan Orogen of Asia: structural and thermal evolution of the lower and upper plates. *Geological Association of Canada, Program with Abstracts* **30**, 188.

St-Onge, M. R., Scott, D. J., Corrigan, D. & Wodicka, N. (2005*b*). Geological maps and descriptive notes and legend, central Baffin Island area, Nunavut. *Geological Survey of Canada Maps* **2077A to 2082A**, scale 1:100 000.

Stüwe, K. (1997). Effective bulk composition changes due to cooling: a model predicting complexities in retrograde reaction textures. *Contributions to Mineralogy and Petrology* **129**, 43–52.

Thériault, R. J., St-Onge, M. R. & Scott, D. J. (2001). Nd isotopic and geochemical signature of the Paleoproterozoic Trans-Hudson Orogen, southern Baffin Island, Canada: implications for the evolution of eastern Laurentia. *Precambrian Research* **108**, 113–138.

Tinkham, D. K., Zuuaga, C. A. & Stowell, H. H. (2003). Metapelite phase equilibria modelling in MnNCKFMASH: the effect of variable Al_2O_3 and $MgO/(MgO+FeO)$ on mineral stability. *American Mineralogist* **88**, 1174.

Treloar, P. J., Rex, D. C., Guise, P. G., Coward, M. P., Searle, M. P., Windley, B. F., Petterson, M. G., Jan, M. Q. & Luff, I. W. (1989). K–Ar and Ar–Ar geochronology of the Himalayan collision in NW Pakistan: constraints on the timing of suturing, deformation, metamorphism and uplift. *Tectonics* **8**, 881–909.

Vannay, J.-C. & Hodges, K. V. (1996). Tectonometamorphic evolution of the Himalayan metamorphic core between the Annapurna and

Downloaded from http://petrology.oxfordjournals.org/ by guest on June 7, 2013

Dhaulagiri, central Nepal. *Journal of Metamorphic Geology* **14**, 635–656.

Walker, J. D., Martin, M. W., Bowring, S. A., Searle, M. P., Waters, D. J. & Hodges, K. V. (1999). Metamorphism, melting and extension: age constraints from the High Himalayan Slab of Southeast Zanskar and Northwest Lahaul. *Journal of Geology* **107**, 473–495.

Weinberg, R. F. & Dunlap, W. J. (2000). Growth and deformation of the Ladakh Batholith, northwest Himalayas: implication for timing of continental collision and origin of calc-alkaline batholith. *Journal of Geology* **108**, 303–320.

White, R. W., Powell, R. & Holland, T. J. B. (2001). Calculation of partial melting equilibria in the system Na_2O–CaO–K_2O–FeO–MgO–Al_2O_3–SiO_2–H_2O (NCKFMASH). *Journal of Metamorphic Geology* **19**, 139–153.

Wodicka, N. & Scott, D. J. (1997). A preliminary report on the U–Pb geochronology of the Meta Incognita Peninsula, southern Baffin Island, Northwest Territories. *Geological Survey of Canada Paper* **1997-C**, 167–178.

Wodicka, N. & St-Onge, M. R. (1998). Implications of U–Pb geochronology for the thermal evolution of supracrustal rocks from the Baffin segment of the Trans-Hudson Orogen. *Geological Association of Canada, Program with Abstracts* **23**, A200.

Wodicka, N., Ketchum, J. W. F. & Jamieson, R. A. (2000). Grenvillian metamorphism of monocyclic rocks, Georgian Bay, Ontario, Canada: implications for convergence history. *Canadian Mineralogist* **38**, 471–510.

Wodicka, N., Madore, L., Larbi, Y. & Vicker, P. (2002*a*). Géochronologie U–Pb de filons-couches mafiques de la Ceinture de Cape Smith et de la Fosse du Labrador. *Séminaire d'information sur la recherche géologique, Programme et résumés 2002. Ministère des Ressources naturelles, Québec* **DV 2002-10**, 48.

Wodicka, N., St-Onge, M. R., Scott, D. J. & Corrigan, D. (2002*b*). *Preliminary report on the U–Pb geochronology of the northern margin of the Trans-Hudson Orogen, central Baffin Island, Nunavut. Geological Survey of Canada Paper* **2002-F7**, , 12 pp.

York, D. (1969). Least squares fitting of a line with correlated errors. *Earth and Planetary Science Letters* **5**, 320–324.

Zhao, G., Cawood, P. A., Wilde, S. A. & Min Sun, (2002). Review of global 2·1–1·8 Ga orogens: implications for a pre-Rodinia supercontinent. *Earth-Science Reviews* **59**, 125–162.

Zhu, X. K., O'Nions, R. K., Belshaw, N. S. & Gibb, A. J. (1997). Significance of *in situ* SIMS chronometry of zoned monazite from the Lewisian granulites, northwest Scotland. *Chemical Geology* **135**, 35–53.

Downloaded from http://petrology.oxfordjournals.org/ by guest on June 7, 2013